# Lewis Base-Mediated Stabilization of the Lattice Oxygen Mechanism in $RuO_2$ for Robust Acidic Water Oxidation

**Sheng Hu[1], Siyang Luo[1], Haoxin Du[1], Xiongfeng Zeng[1], Jiao Yang[2], Xing Wang[1]*, Haifeng Bao[1]*, Na Yao[1]***

## Affiliation

[1]State Key Laboratory of New Textile Materials and Advanced Processing, School of Materials Science and Engineering, Wuhan Textile University, Wuhan 430200, P. R. China.

[2]School of Physics and Engineering, Henan University of Science and Technology, Luoyang, 471023, China.

## *Corresponding author

*Correspondence to: wx@wtu.edu.cn (X. Wang); baohaifeng@wtu.edu.cn (H. Bao); yaona@wtu.edu.cn (N. Yao),

# 1. Experimental section

### Chemicals

All chemicals were used as received. Ruthenium(III) chloride ($RuCl_3$, ≥99.9%), aluminium chloride ($AlCl_3$, ≥99%), gallium chloride ($GaCl_3$, ≥99%), indium chloride ($InCl_3$, ≥99%), Vulcan XC 72 carbon, absolute ethanol ($C_2H_6O$, ≥99.7%), Nafion117 (≈5%), and isopropanol ($C_3H_8O$, ≥99.7%) were purchased from Macklin, Ltd. Carbon cloth (WOS 1011) was obtained from CeTech. High-purity water was acquired from the Milli-Q purification system.

### Fabrication of M-$RuO_2$ (M=Al, Ga, In )

Briefly, 0.5 mmol of $RuCl_3$ and 0.02 mmol of the respective metal chloride ($InCl_3$, $AlCl_3$, or $GaCl_3$) were dissolved in 5 mL of absolute ethanol. The solution was stirred thoroughly to ensure homogeneity. Subsequently, the mixture was transferred to a muffle furnace and heated to 600 °C at a ramp rate of 5 °C/min, maintained at this temperature for 120 min, and subsequently cooled to room temperature at the same ramp rate (5 °C/min). The synthesis of In-RuO2-x (x=1, 2, 3, or 4) followed the same procedure as the synthesis method, with different Se powder contents (0, 0.01, 0.02, 0.03 and 0.04 mmol, respectively) in anhydrous ethanol.

### Fabrication of $RuO_2$

The synthesis of $RuO_2$ was conducted using an identical protocol to that of M-$RuO_2$, excluding the addition of any foreign metal chlorides.

# 2. Material Characterizations

X-ray diffraction (XRD) patterns were recorded on a Rigaku D/Max-2500 with Cu Kα radiation (λ = 1.5408 Å), scanning a 2θ range of 5-85°. scanning electron microscopy (SEM) images were collected on a JEOL JSM-7500F) and transmission electron microscopy (TEM) images were collected on a Talos F200X G2 AEMC. Elemental analysis was performed using inductively coupled plasma mass spectrometer (ICP-MS) on an Agilent 7700 instrument. X-ray photoelectron spectroscopy (XPS) spectra were

conducted on a Thermo Scientific K-Alpha+PHI5000 instrument. Ru K-edge were acquired at 1W1B station in Beijing Synchrotron Radiation Facility (BSRF). The facility operated with a storage ring energy of 2.5 GeV and a typical current of 250 mA. Data were recorded in transmission mode under ambient conditions, utilizing a Si(111) double-crystal monochromator and ionization chambers. Subsequent data processing was conducted using the Demeter software suite. Specifically, the Athena module was used for spectral normalization, while Artemis was utilized for shell fitting in R-space based on the Fourier-transformed $k^3$ weighted $\chi(k)$functions.

## 3. In situ Raman

In situ Raman spectra were observed using a confocal micro-Raman spectrometer (DXR microscope) and a flow electrochemical reaction cell. The test was carried out with a 10× objective lens and a 2.0 mW excitation laser. In-$RuO_2$/Au (working electrode), a platinum wire (counter electrode), and a saturated calomel electrode (reference electrode) (acidic solution of 0.5 M $H_2SO_4$) were used as the working electrode, reference electrode (AgCl/Ag), and reference electrode, respectively. The flow rate of the electrolyte was 5 mL $min^{-1}$ to remove the oxygen produced in the reaction process. The sample information was collected after a constant potential was applied for 20 s, and the in situ Raman spectra of each working electrode were recorded three times. In the voltage range from the open-circuit potential (OCP) to 1.7 V vs. RHE, a change in the Raman spectra was observed.

## 4. In situ ATR-SEIRAS

In-situ attenuated total reflection surface enhanced infrared absorption spectroscopy (ATR-SEIRAS) tests were conducted to detect reaction intermediates during the oxygen evolution reaction (OER) in order to verify the reaction mechanism. In situ FTIR experiments were performed using a custom-built three-electrode electrochemical cell. The catalysts were loaded onto a fixed-angle Au coated Si electrode embedded in the centre of the cell, while a Pt wire and saturated reference electrode (Ag/AgCl) served as the counter and reference electrodes, respectively.

During the OER process, potentials were applied from the OCP to 1.8 V vs. RHE under constant voltage, and the SR-FTIR spectra were recorded by averaging 100 scans at a resolution of 1 $cm^{-1}$. The background spectrum of the working electrode was recorded under open-circuit conditions, and the recorded spectra were processed using the OMNIC software.

## 5. Electrochemical measurement

All electrochemical measurements were conducted using the Chenhua CHI-760E electrochemical workstation. A saturated calomel electrode (SCE, $Hg/Hg_2Cl_2$) served as the reference electrode in 0.5 M $H_2SO_4$ for the oxygen evolution reaction (OER) test, and a graphite rod was utilized as the counter electrode. To prepare the working electrode, 3 mg of M-$RuO_2$ was dispersed in 600 μL of 0.1% Nafion solution (diluted with isopropanol) and ultrasonicated for 30 min to disperse uniformly, after which 9 μL was dropped on a glassy carbon (GC) electrode. All potentials were calibrated relative to the reversible hydrogen electrode (RHE) potentials without iR compensation: E (vs. RHE) = E (vs. $Hg/Hg_2Cl_2$) + 0.059*pH + 0.241 V. Linear sweep voltammetry (LSV) was conducted at a scan rate of 10 mV $s^{-1}$ for the polarization curves. For measurements of double-layer capacitances (Cdl), cyclic voltammetry (CV) cycling was performed at different scanning rates of 10, 20, 30, 40, and 50 mV $s^{-1}$ within the non-faradic region. Electrochemical impedance spectroscopy (EIS) was performed over frequencies ranging from 100 kHz to 0.01 Hz with input voltages of 1.25 V, 1.3 V, 1.35 V, 1.4 V, 1.45 V, 1.5 V, and 1.55 V. Electrochemically active surface areas (ECSA) were measured by cyclic voltammetry (CV) in the potential window from 1 to 1.1 V vs. SCE at scan rates of 10, 20, 30, 40, and 50 mV $s^{-1}$. The current density at 1.05 V vs. SCE was used to calculate the ECSA. The electrical double-layer capacitance ($C_{dl}$) was calculated by the equation $C_{dl} = (ja-jc)/2\nu$, where ja and jc are the anodic current density and cathodic current density, respectively, and ν is the scan rate. Thus, $C_{dl}$ is the slope of the linear relationship between (ja-jc)/2 and the scan rate. The ECSA can be calculated as $ECSA = C_{dl}/C_s$.

## 6. PEMWE electrolyser

For the anode, the mixture of 40 mg electrocatalyst, 0.5 mL Nafion (5 wt%), 7 mL DI water and 2.5 mLethanol was ultrasonic dispersion for about 2 h to form an aqueous solution. For the cathode, 40 *wt.*% Pt/C as the electrocatalyst and the other steps of ink preparation were the same as for the anode. The catalyst ink was sprayed onto the proton exchange membrane (N115). The assembly was dealed with hot pressing at 130 °C, and the pressure was maintained at 3 MPa for 3 min. The I-V curves and long-term stability were performed at the temperature of 20 °C, 40 °C, 60 ℃ and 80 ℃ under pure water conditions.

## 6. DFT calculation

DFT calculations were conducted using the Vienna Ab-initio Simulation Package (VASP). The Perdew-Burke-Ernzerhof (PBE) functional of the generalized gradient approximation (GGA) with projector augmented wave (PAW) was employed to describe the exchange-correlation function. A plane-wave basis kinetic energy cutoff of 520 eV was applied, and reciprocal space was sampled using a Gamma centered k-mesh with a grid of 3 × 3 × 1. A vacuum layer of at least 15 Å in the z direction was included to decouple interactions between replicated cells. The convergence criterion for the total energy was set to $1\times10^{-5}$ eV atom–1, and the residual Hellmann-Feynman force was limited to 0.02 eV Å–1. Gas-phase $H_2$ and $H_2O$ molecules were optimized within a box with dimensions of 15 × 15 × 15 Å using Gamma point sampling of the Brillouin zone. All crystallographic data for DFT calculations were taken from optimization results. DFT dispersion correction (DFT-D3) method was used to treat the van der Waals interactions. Dipole-field corrections in the potential correction mode were employed to remove spurious interactions between periodic images along the surface normal. The free energies are approximated as follows: $\Delta G = E_{DFT} + \Delta ZPE - T\Delta S$, where EDFT and ZPE are the total and zero-point electronic energies calculated through DFT, and TS are entropic contributions (only taken into 2 account for gas-phase species and intermediate species).

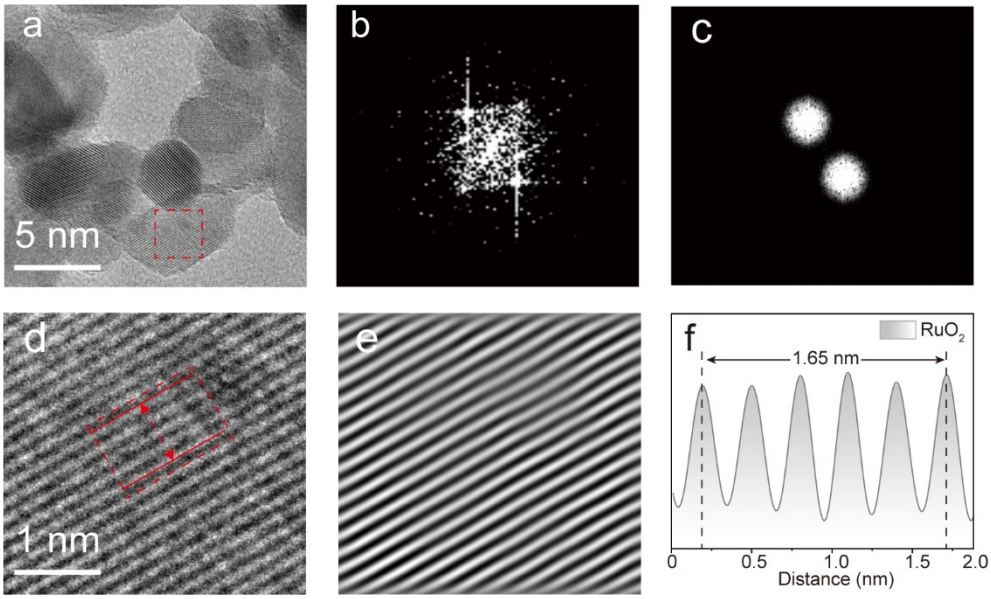


**Fig. S1** TEM image of $RuO_2$.

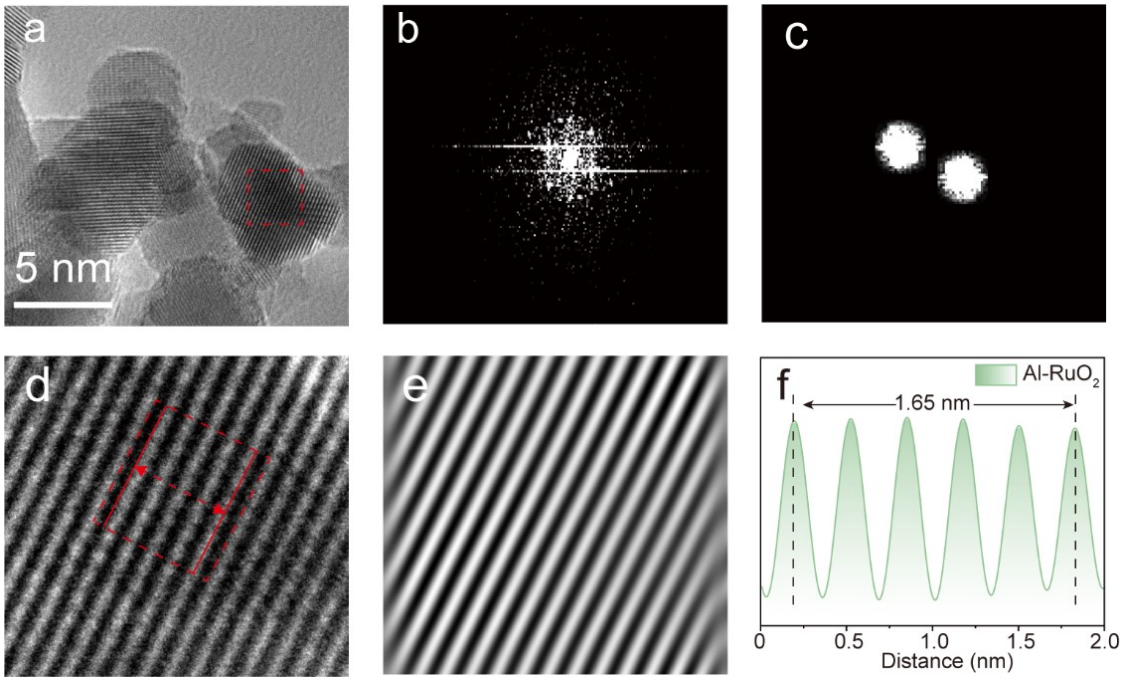


**Fig. S2** TEM image of Al-$RuO_2$.

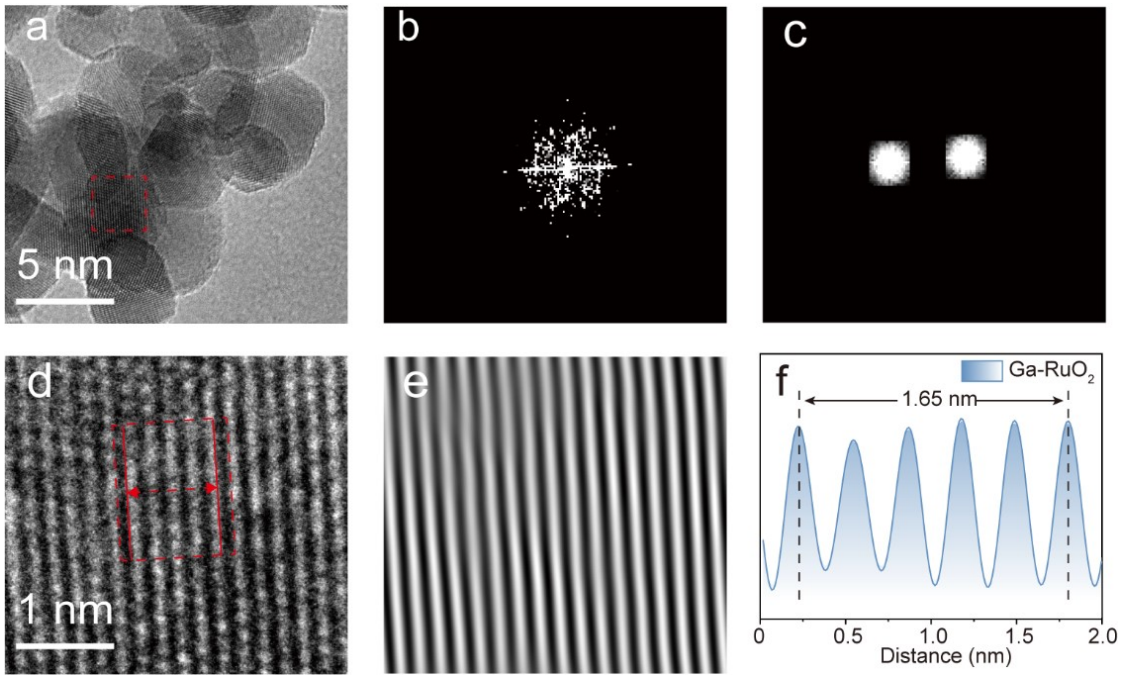


**Fig. S3** TEM image of Ga-$RuO_2$.

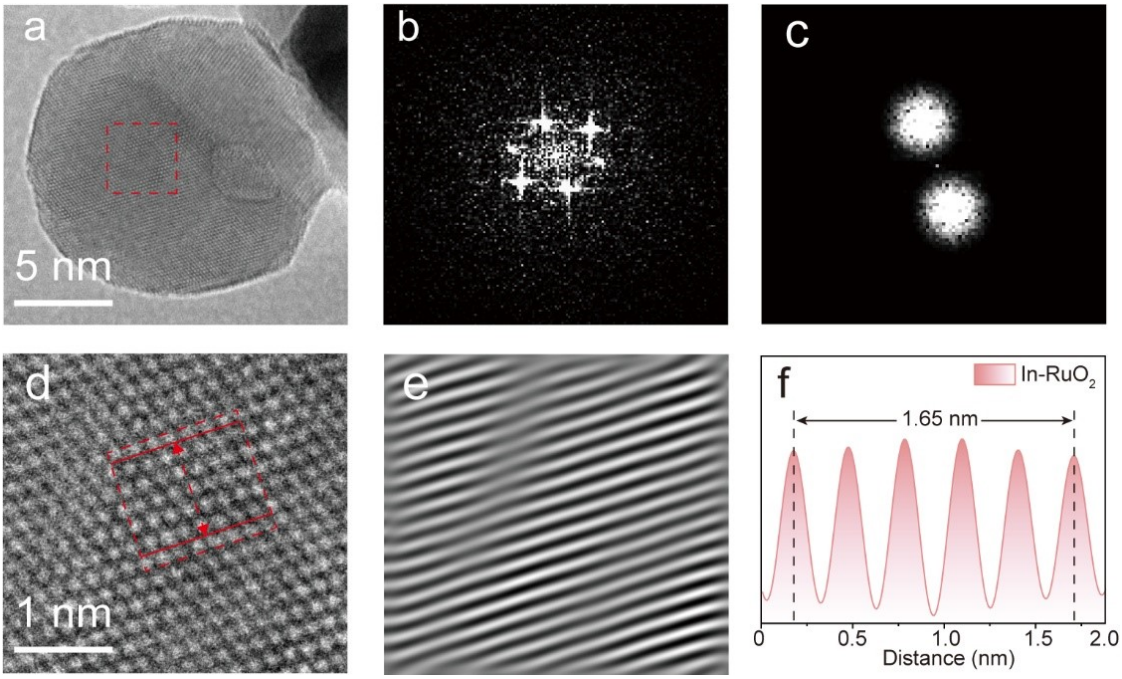


**Fig. S4** TEM image of In-$RuO_2$.

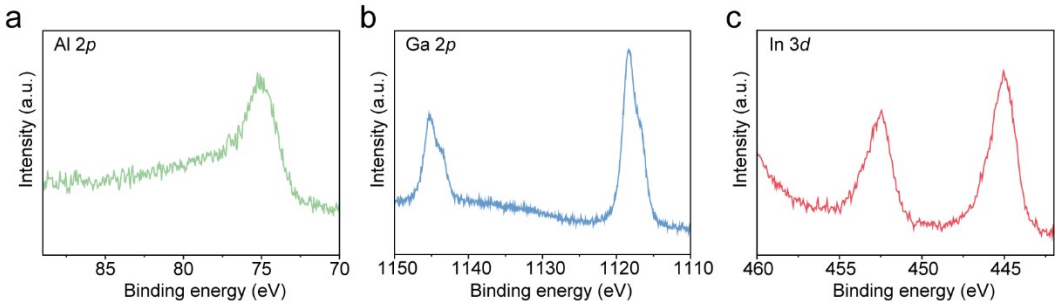


**Fig. S5** The high-resolution XPS spectra of (a) Al 2*p* for Al-$RuO_2$, (b) Ga 2*p* for Ga-$RuO_2$ and (c) In 3*d* for In-$RuO_2$.

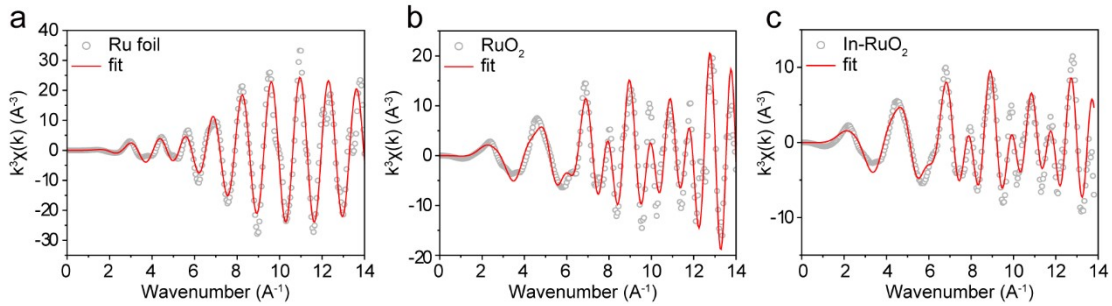


**Fig. S6** Ru K-edge EXAFS fitting curves in k space for (a) Ru foil, (b) $RuO_2$ and (c) In-$RuO_2$.

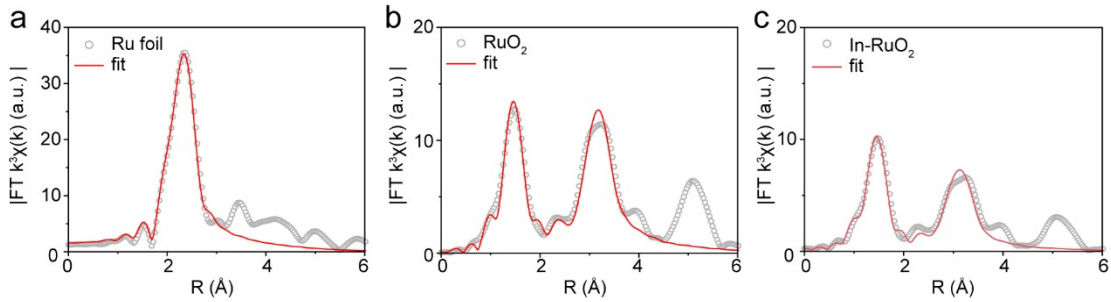


**Fig. S7** Ru K-edge EXAFS fitting curves in R space for (a) Ru foil, (b) $RuO_2$ and (c) In-$RuO_2$.

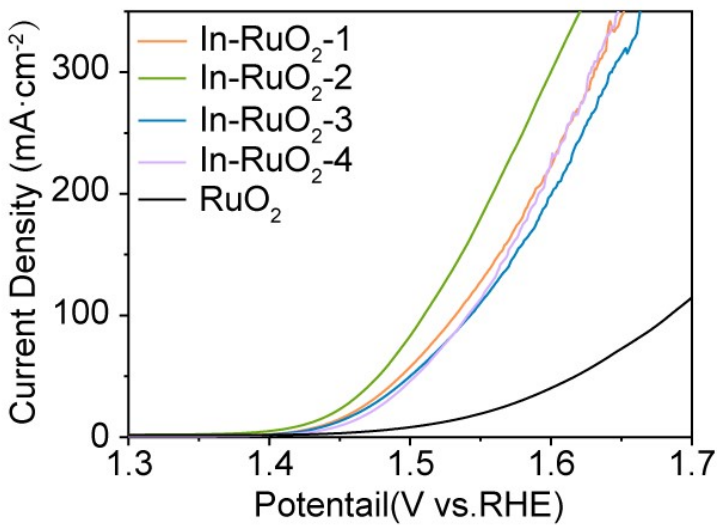


**Fig. S8** LSV curves of In-$RuO_2$ with different In doping amount in 0.5 M $H_2SO_4$ solution.

We synthesized In-$RuO_2$ with various ratios of In doping to determine the effect of In doping ratio (0, 0.01, 0.02, 0.03 and 0.04 mmol) on the OER activity. The samples synthesized by adding 0, 0.01, 0.02, 0.03 and 0.04 mmol $InCl_3$ are named as $RuO_2$, In-$RuO_2$-1, In-$RuO_2$-2, In-$RuO_2$-3 and In-$RuO_2$-4, respectively. In-$RuO_2$-2 exhibits the highest catalytic activity among the In-$RuO_2$ with different doping amounts of In. Therefore, we choose In-$RuO_2$-2 for comparative analysis in the manuscript. Also, In-$RuO_2$-2 represent In-$RuO_2$-2, respectively, in the manuscript.

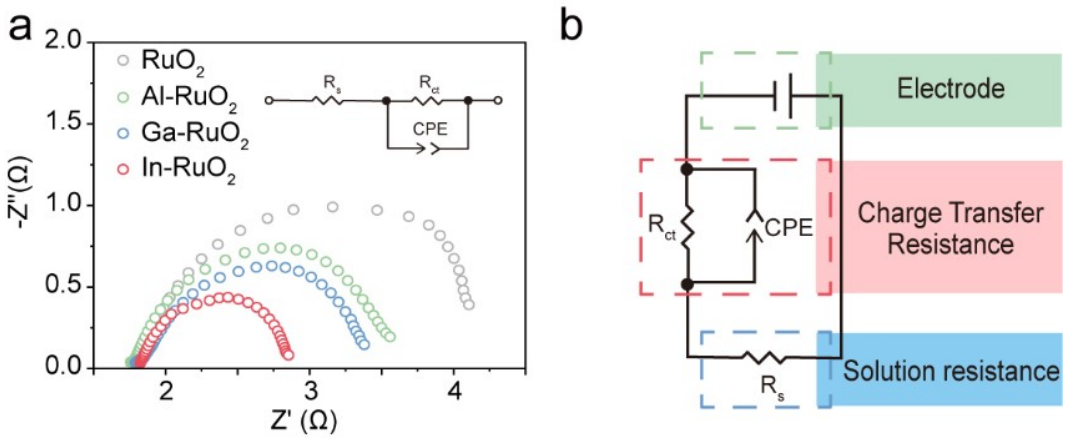


**Fig. S9** (a) Nyquist plots of $RuO_2$, Al-$RuO_2$, Ga-$RuO_2$ and In-$RuO_2$ at 1.5 V vs. RHE. (b) Electrode structure and equivalent circuit diagram.

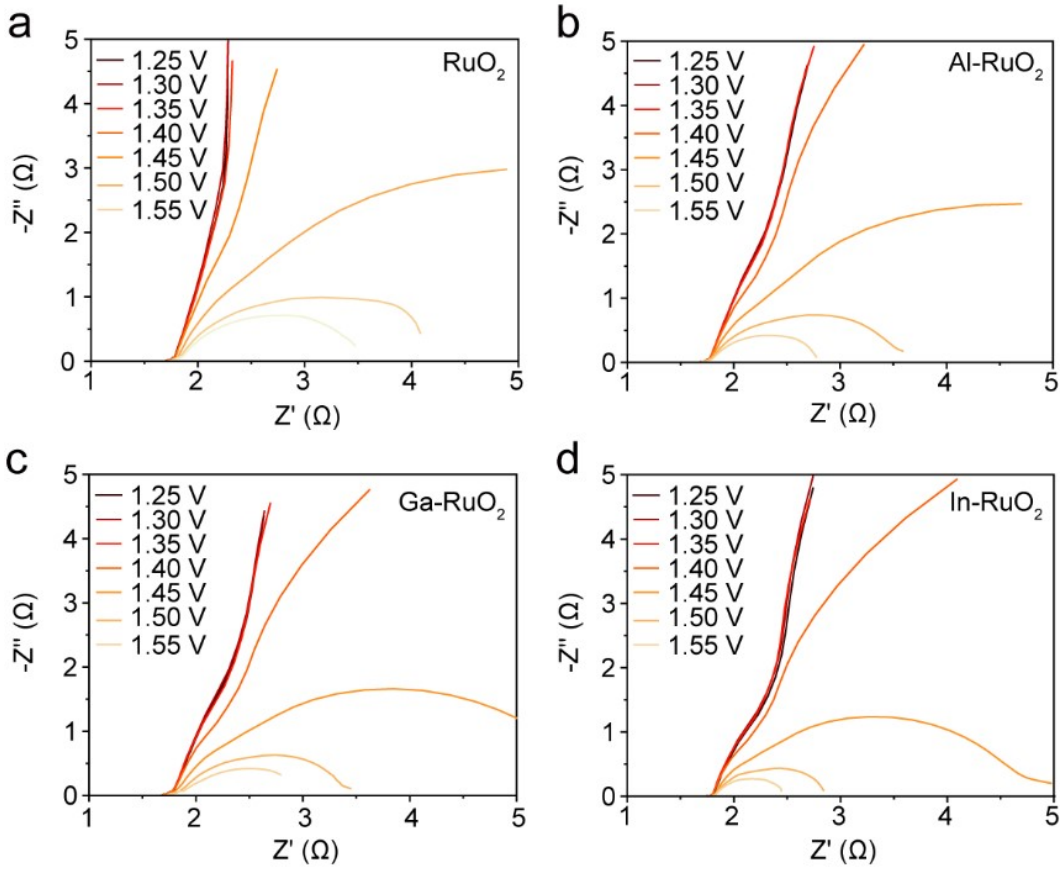


**Fig. S10** Nyquist plots of (a) $RuO_2$, (b) Al-$RuO_2$, (c) Ga-$RuO_2$ and (d) In-$RuO_2$ at different voltages.

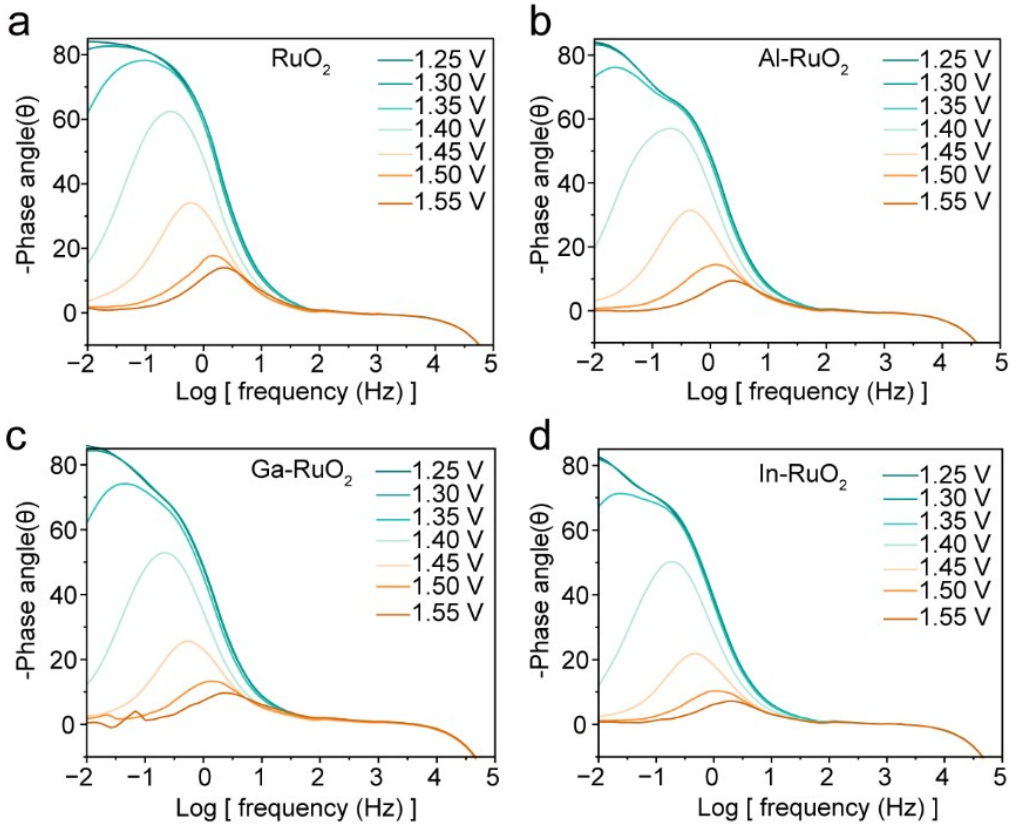


**Fig. S11** Bode phase plots of (a) $RuO_2$, (b) Al-$RuO_2$, (c) Ga-$RuO_2$ and (d) In-$RuO_2$ at different voltages.

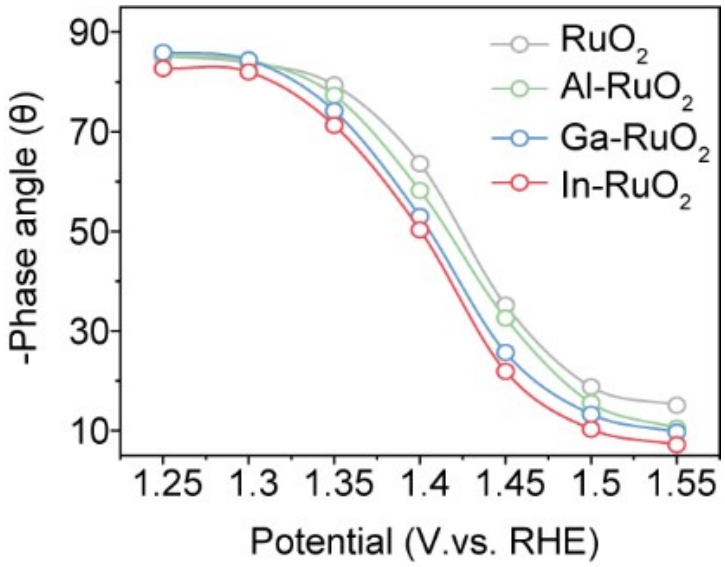


**Fig. S12** Summarized phase peak angles of $RuO_2$ and M-$RuO_2$ at 1.25-1.55 V.

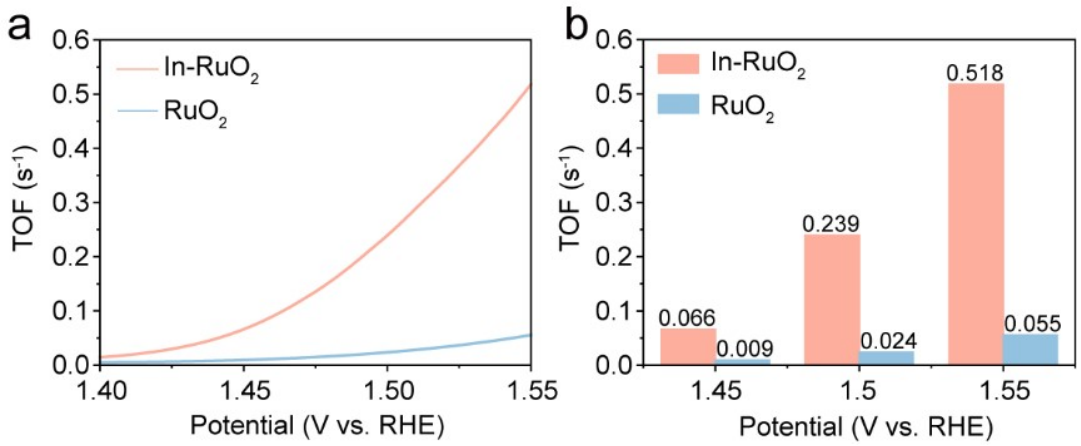


**Fig. S13** Comparison of TOF values of $RuO_2$ and M-$RuO_2$. (a) TOF curves, (b) TOF values of $RuO_2$ and In-$RuO_2$ at different potential.

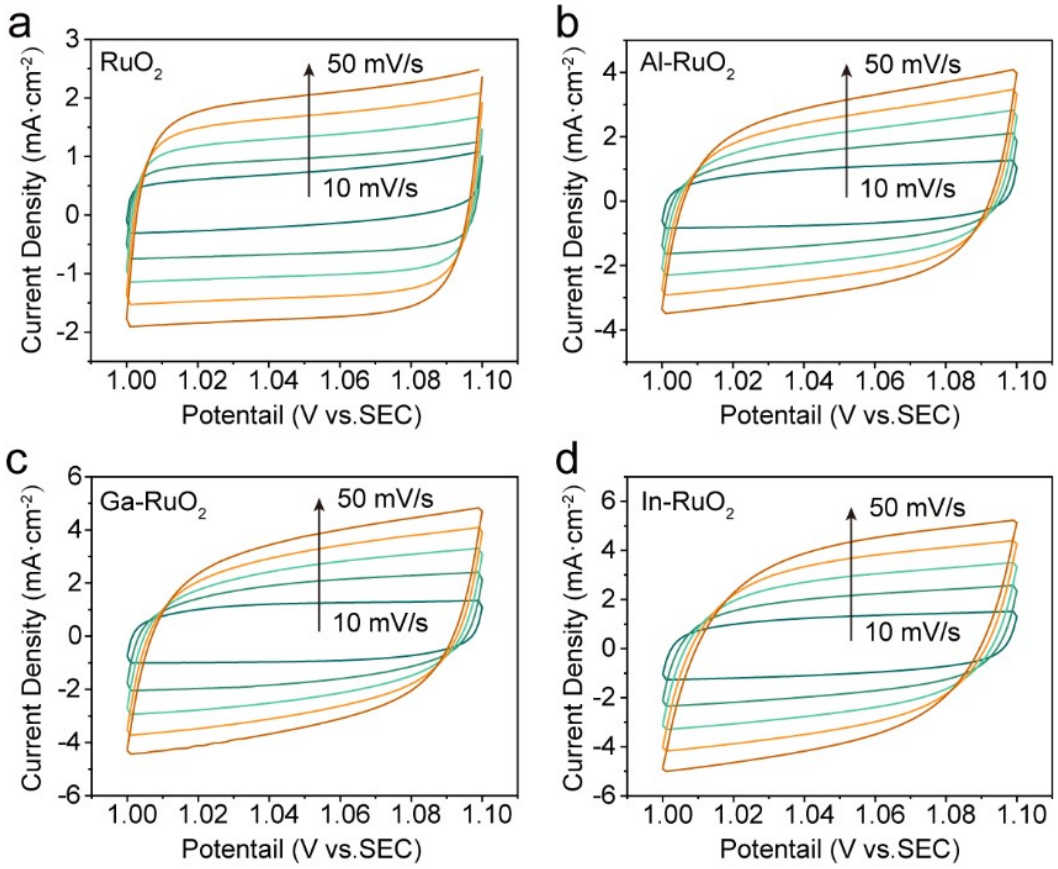


**Fig. S14** CV curves of (a) $RuO_2$, (b) Al-$RuO_2$, (c) Ga-$RuO_2$ and (d) In-$RuO_2$ at different scan rates.

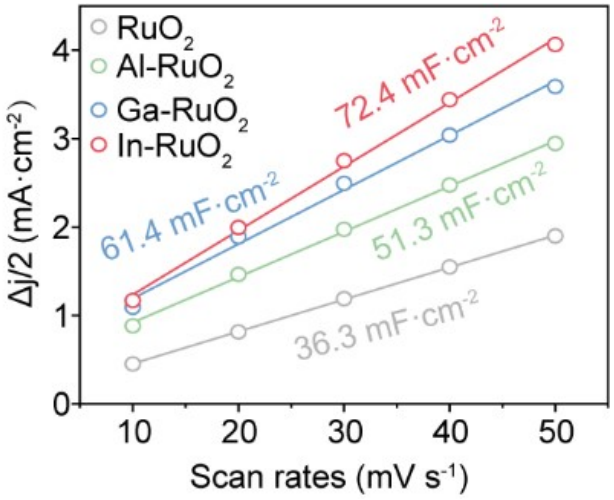


**Fig. S15** The double-layer capacitance values of $RuO_2$, Al-$RuO_2$, Ga-$RuO_2$ and In-$RuO_2$ at different scan rates.

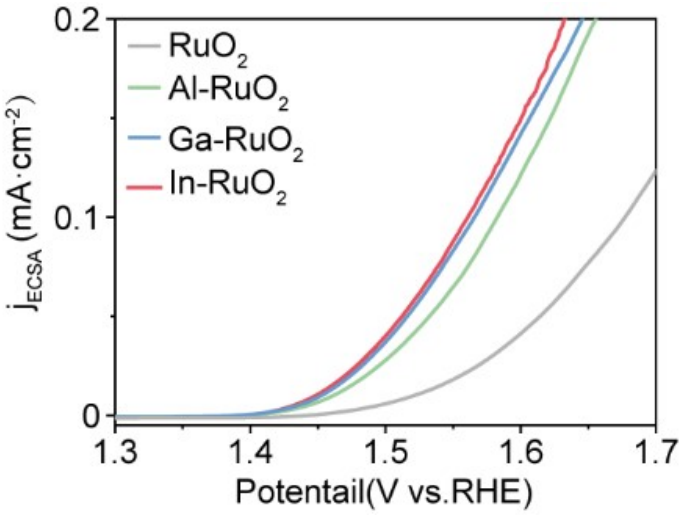


**Fig. S16** LSV curves normalized by ECSA of different catalysts to indicate intrinsic performance.

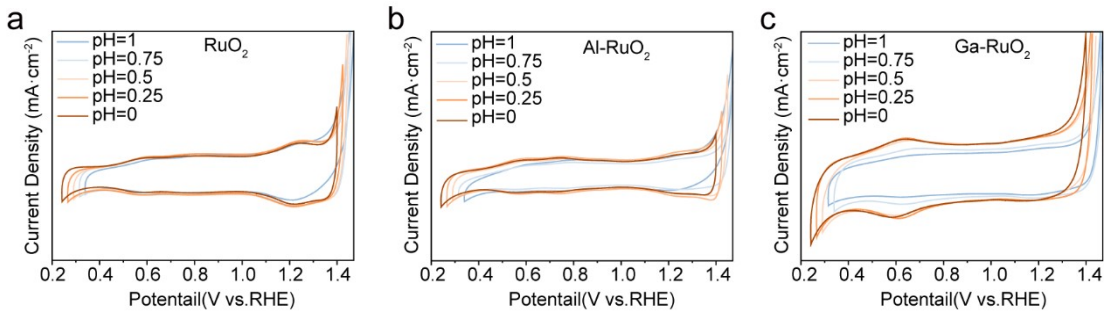


**Fig. S17** pH-dependent test of (a) $RuO_2$, (b) Al-$RuO_2$ and (c) Ga-$RuO_2$ samples.

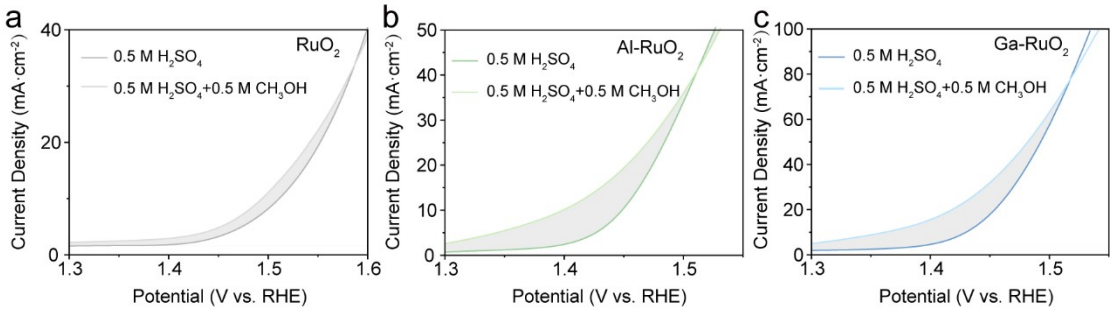


**Fig. S18** LSV curves for (a) $RuO_2$, (b) Al-$RuO_2$ and (c) Ga-$RuO_2$ in 0.5 M $H_2SO_4$ with and without methanol (0.5 M).

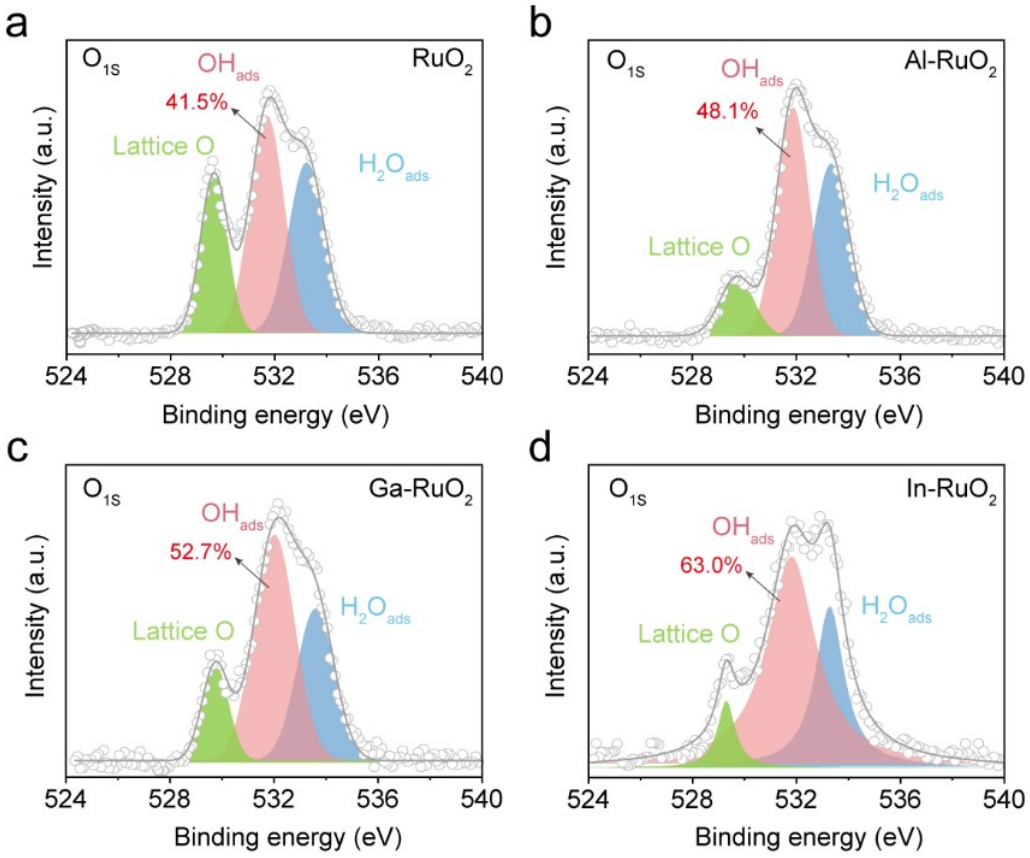


**Fig. S19** The O 1s XPS spectra of (a) $RuO_2$, (b) Al-$RuO_2$, (c) Ga-$RuO_2$ and (d) In-$RuO_2$.

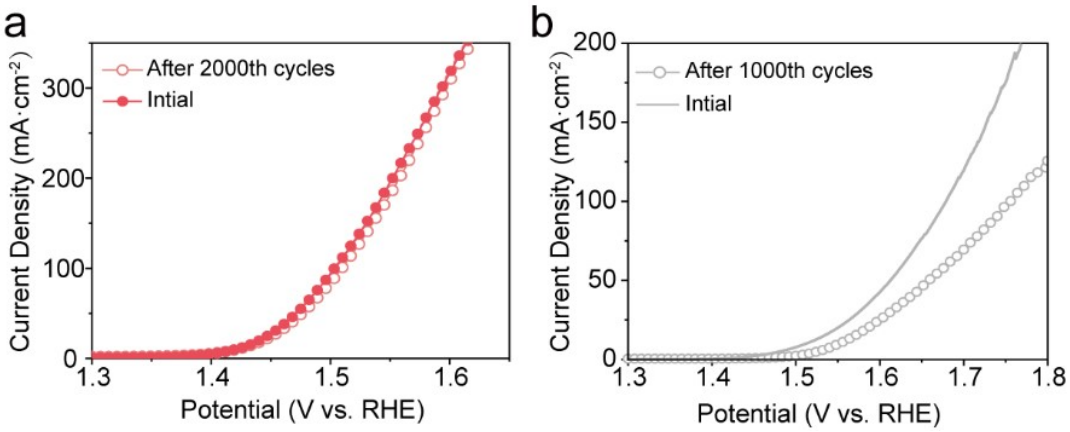


**Fig. S20** (a) LSV curves of initial and after 2000 CV cycles on In-$RuO_2$. (b) LSV curves of initial and after 1000 CV cycles on $RuO_2$.

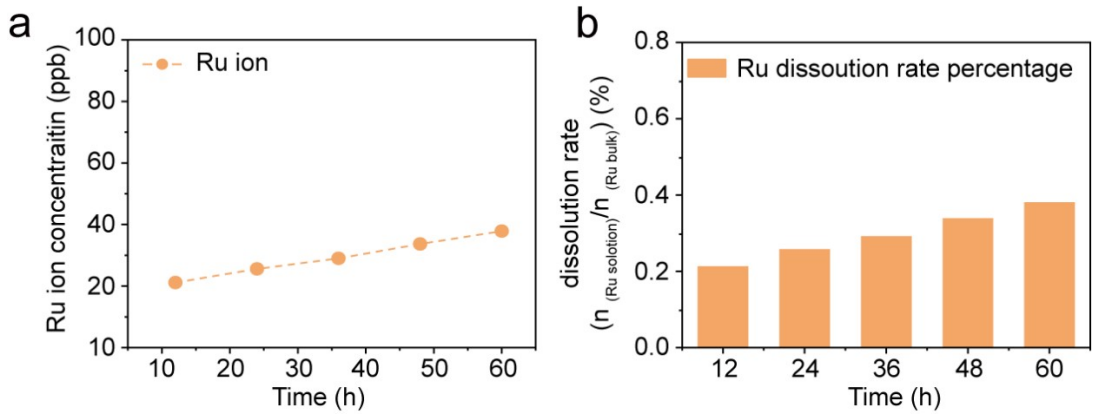


**Fig. S21** (a) Dissolved Ru ion concentration in electrolyte for In-$RuO_2$ determined via ICP-MS. (b) The dissolution rate percentage of Ru in In-$RuO_2$ catalysts n ($Ru_{solotion}$) is the Ru contents in solution and n ($Ru_{bulk}$) is the Ru contents in catalysts.

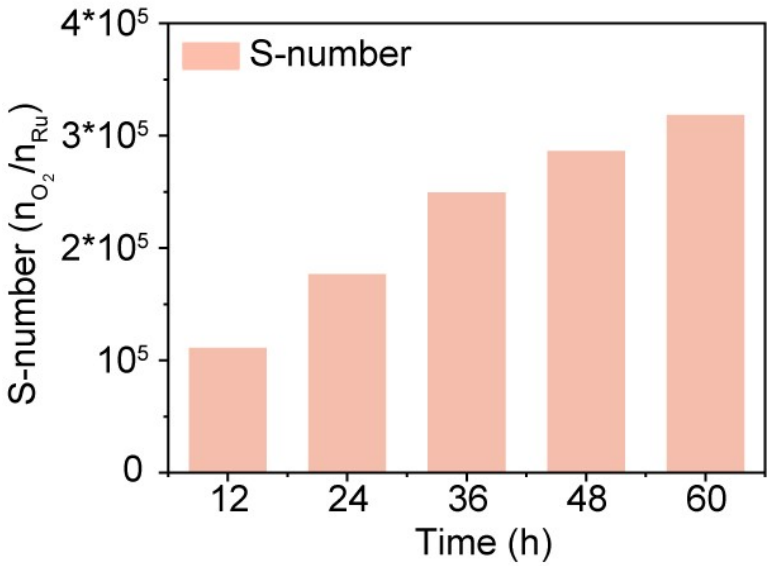


**Fig. S22** S-number for In-$RuO_2$ with change of reaction time.

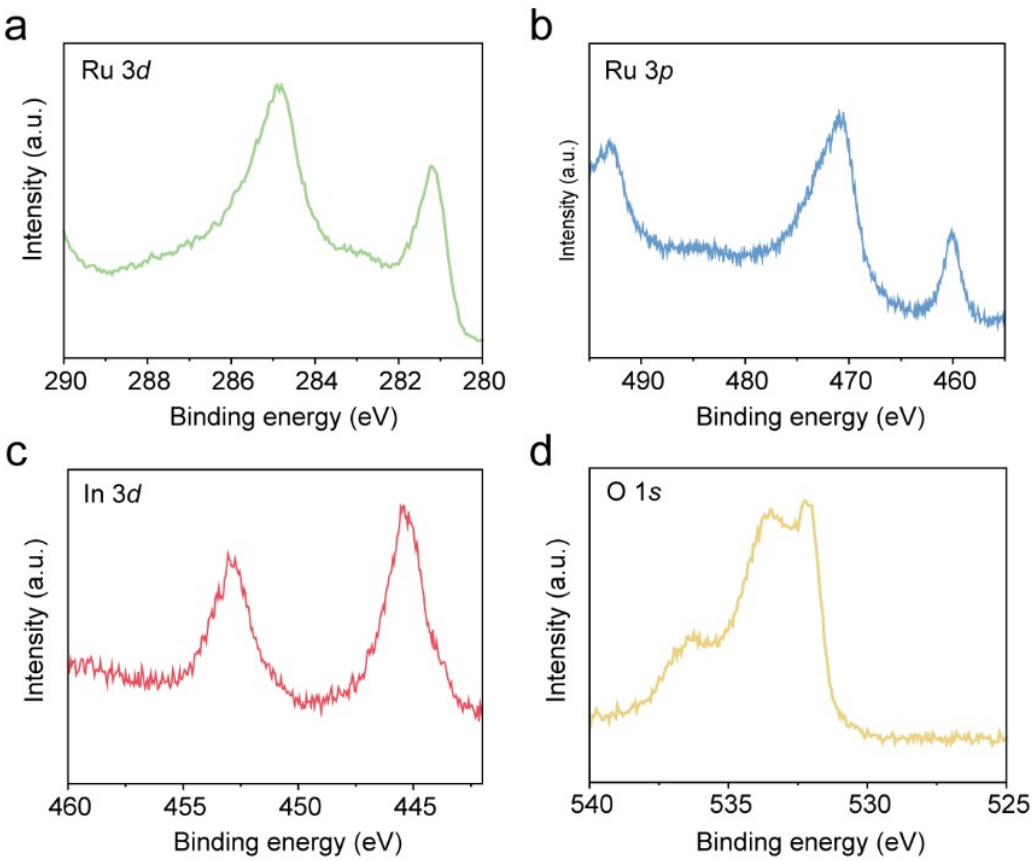


**Fig. S23** XPS spectra of (a) Ru 3*d* for In-$RuO_2$, (b) Ru 3*p* for In-$RuO_2$, (c) In 3*d* for In-$RuO_2$ and (d) O 1*s* for In-$RuO_2$.

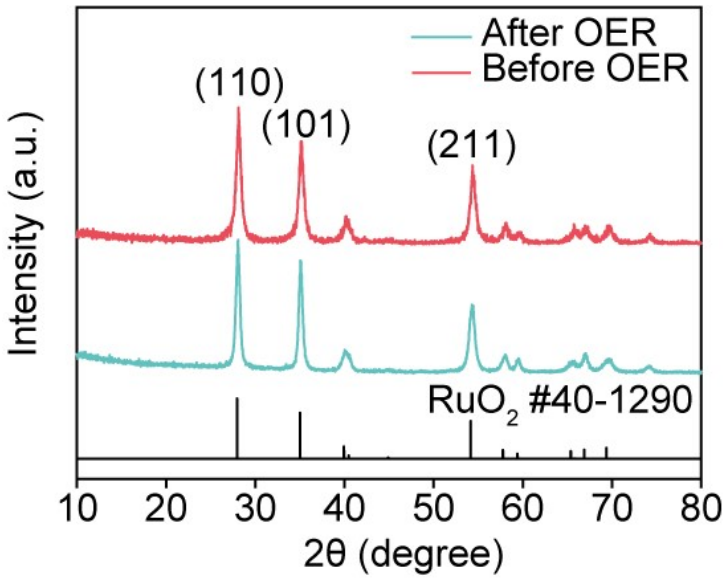


**Fig. S24** The XRD pattern of In-$RuO_2$ after OER testing.

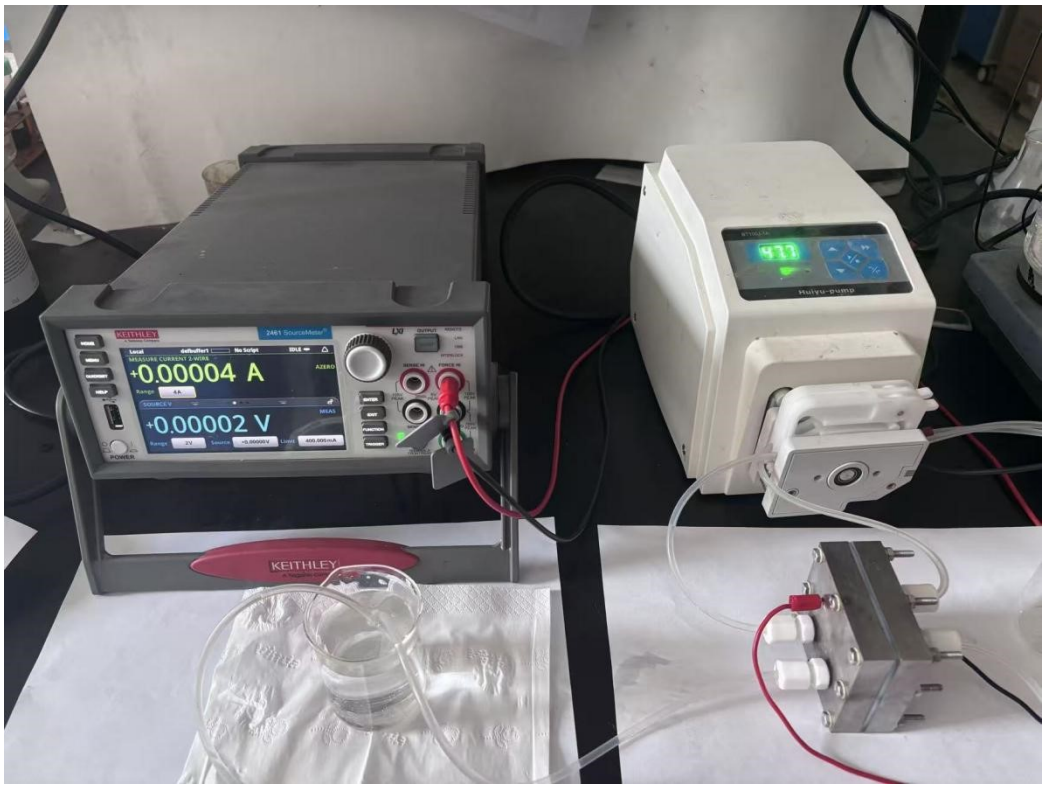


**Fig. S25** Actual picture of PEMWE device.

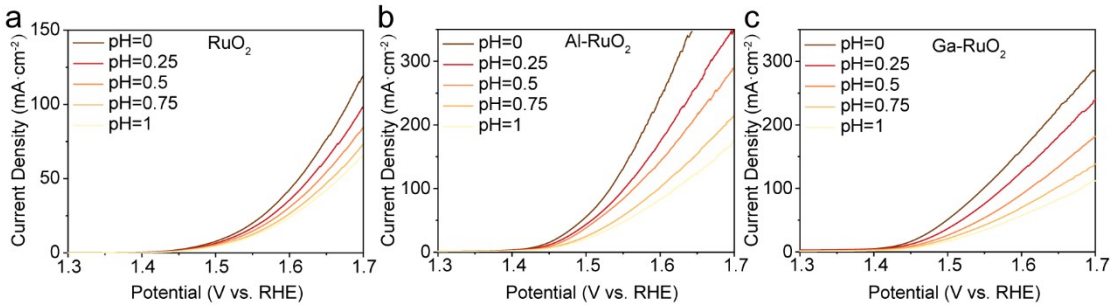


**Fig. S26** LSV curves of the as-prepared samples in electrolyte with different pH value (a) $RuO_2$, (b) Al-$RuO_2$ and (c) Ga-$RuO_2$.

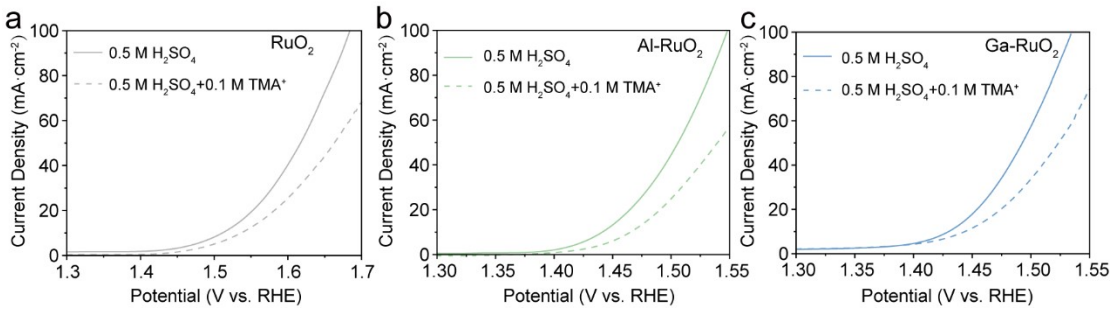


**Fig. S27** OER polarization curves of (a) $RuO_2$, (b) Al-$RuO_2$ and (c) Ga-$RuO_2$ in 0.5 M $H_2SO_4$ electrolyte with and without $TAM^+$.

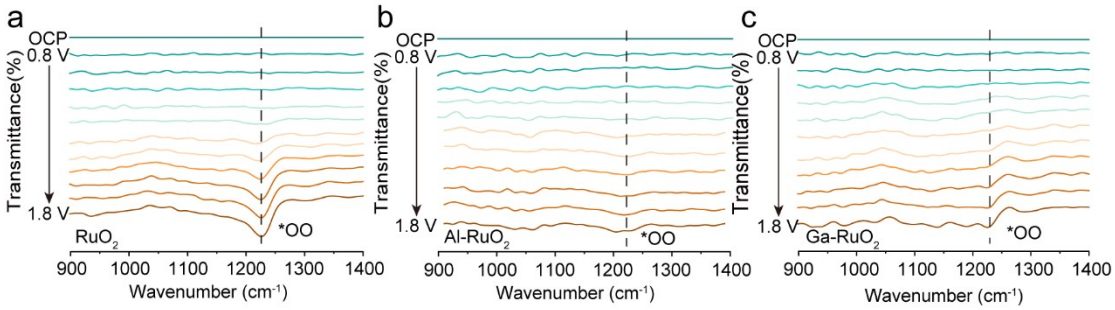


**Fig. S28** In-situ ATR-SEIRAS spectra of (a) $RuO_2$, (b) Al-$RuO_2$ and (c) Ga-$RuO_2$ during OER.

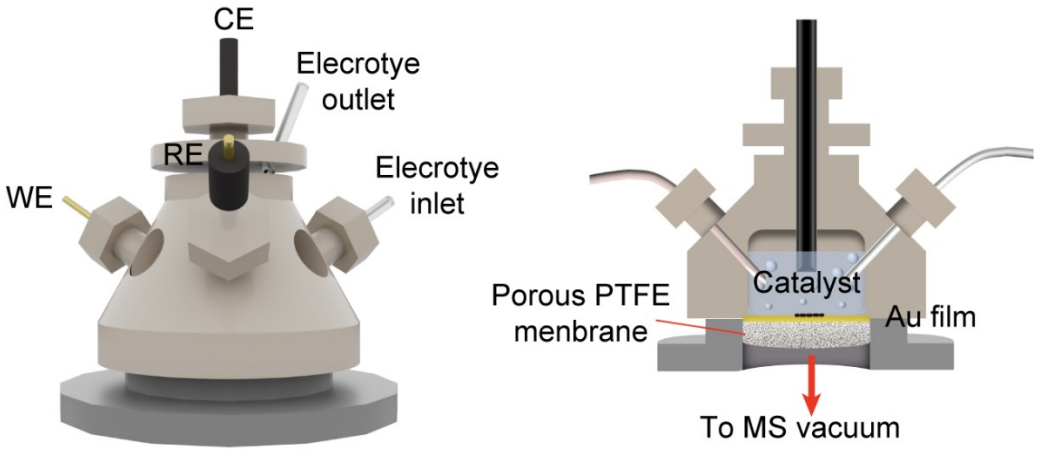


**Fig. S29** DEMS device diagram.

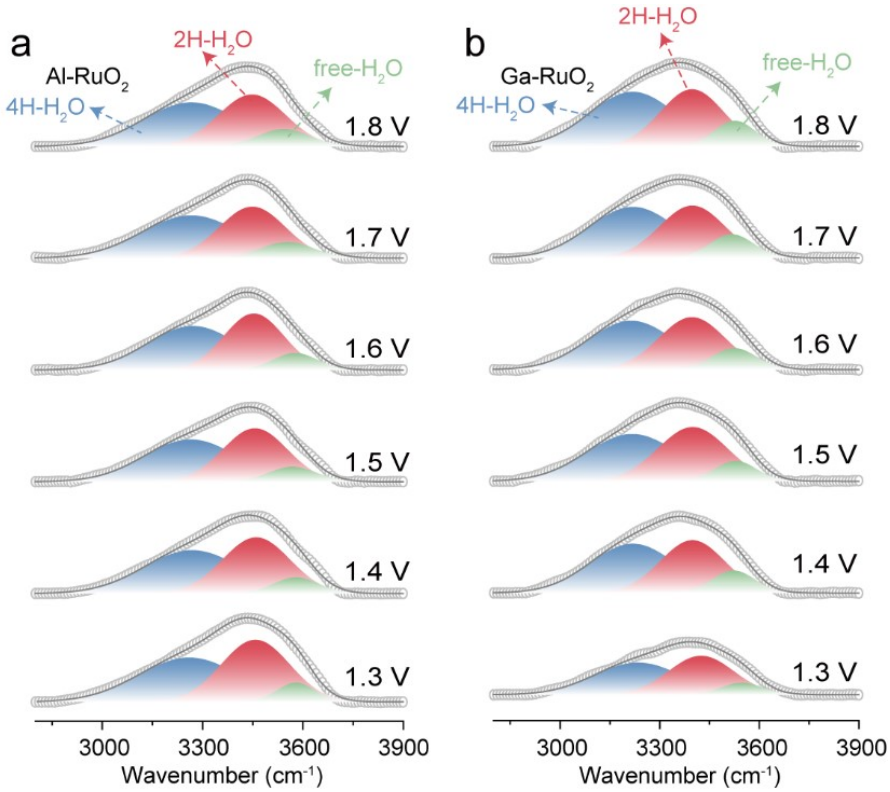


**Fig. S30** In-situ ATR-SEIRAS spectra were recorded at potentials from 1.3 V to 1.8 V on (a) Al-$RuO_2$ and (b) Ga-$RuO_2$.

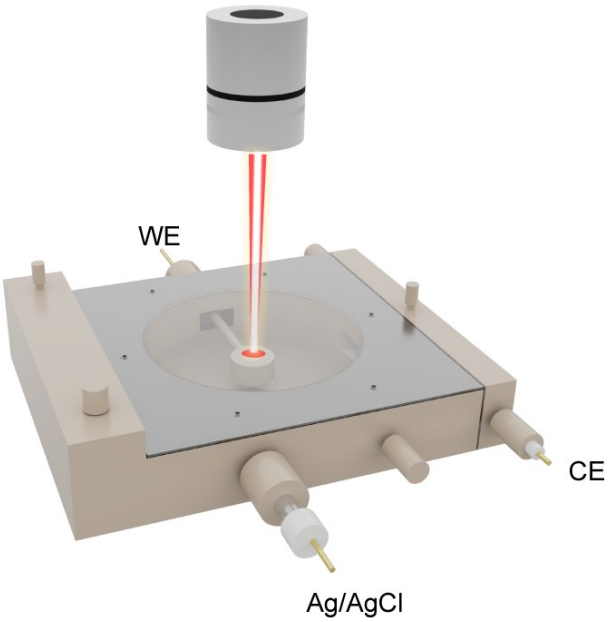


**Fig. S31** In-situ Raman device diagram.

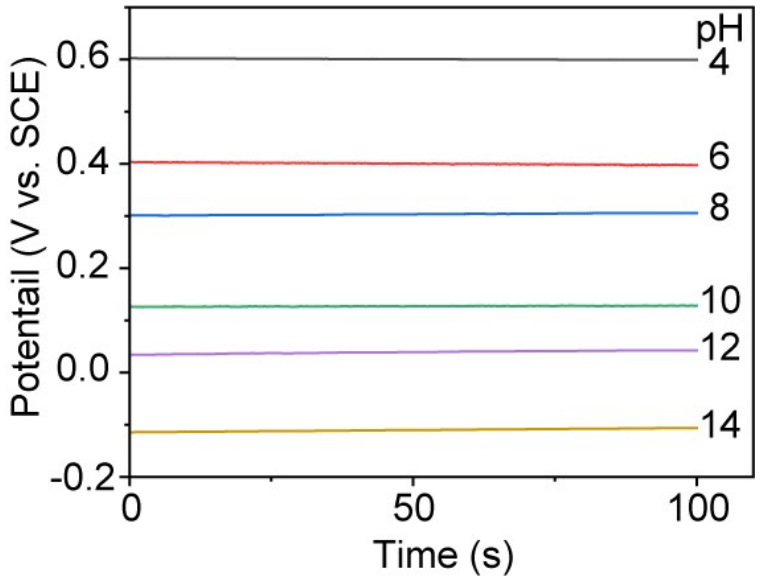


**Fig. S32** Time dependence of OCP of the $IrO_x$ electrodeposited electrode on different pH.

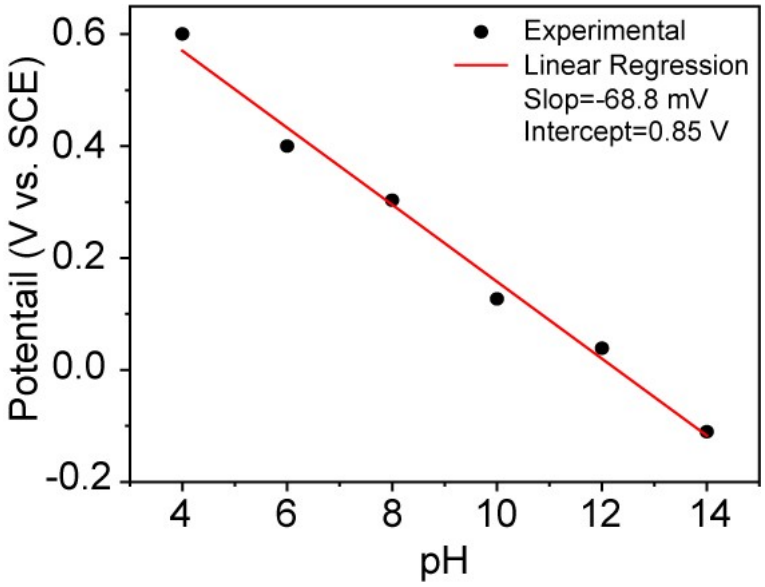


**Fig. S33** pH dependence of OCP of $IrO_x$ electrodeposited electrode.

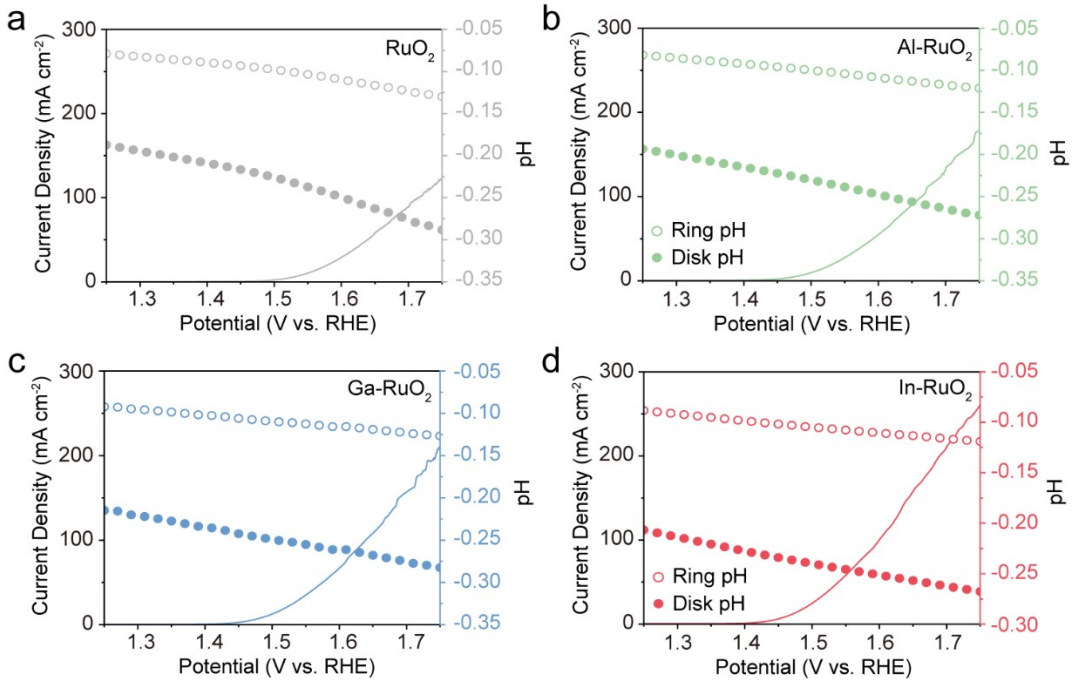


**Fig. S34** OER polarization curves of (a) $RuO_2$, (b) Al-$RuO_2$, (c) Ga-$RuO_2$, (d) In-$RuO_2$ and corresponding local pH under potential.

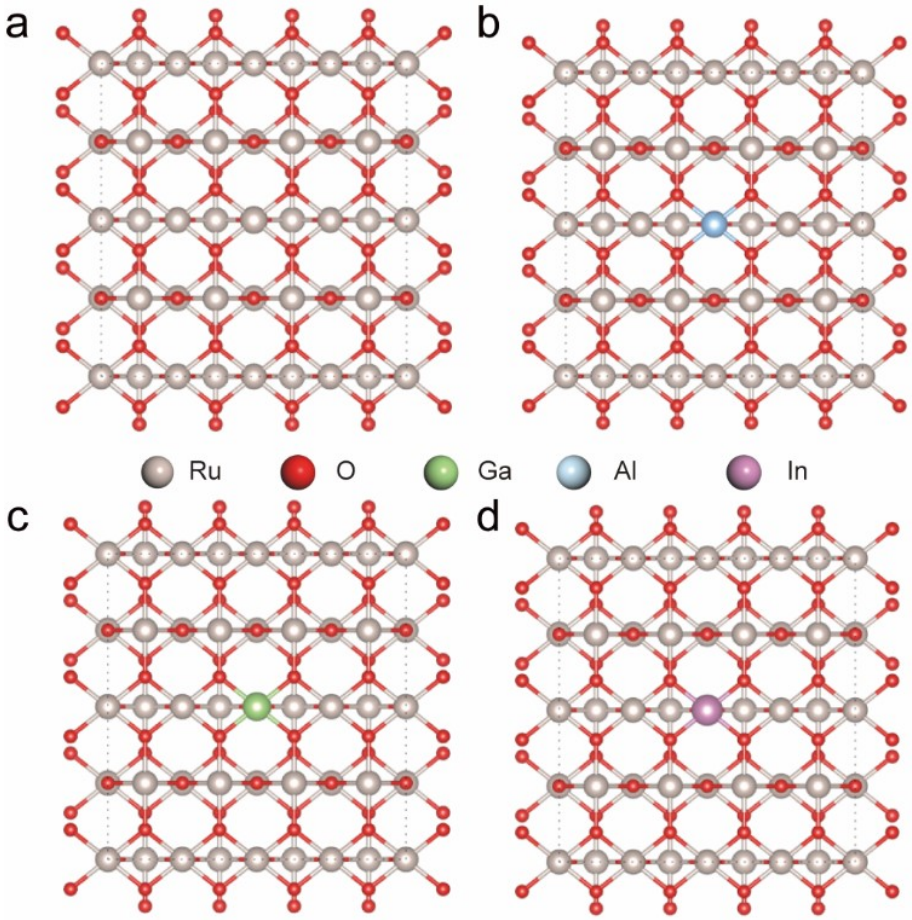


**Fig. S35** The geometric configurations for (a) $RuO_2$, (b) Al-$RuO_2$, (c) Ga-$RuO_2$ and (d) In-$RuO_2$.

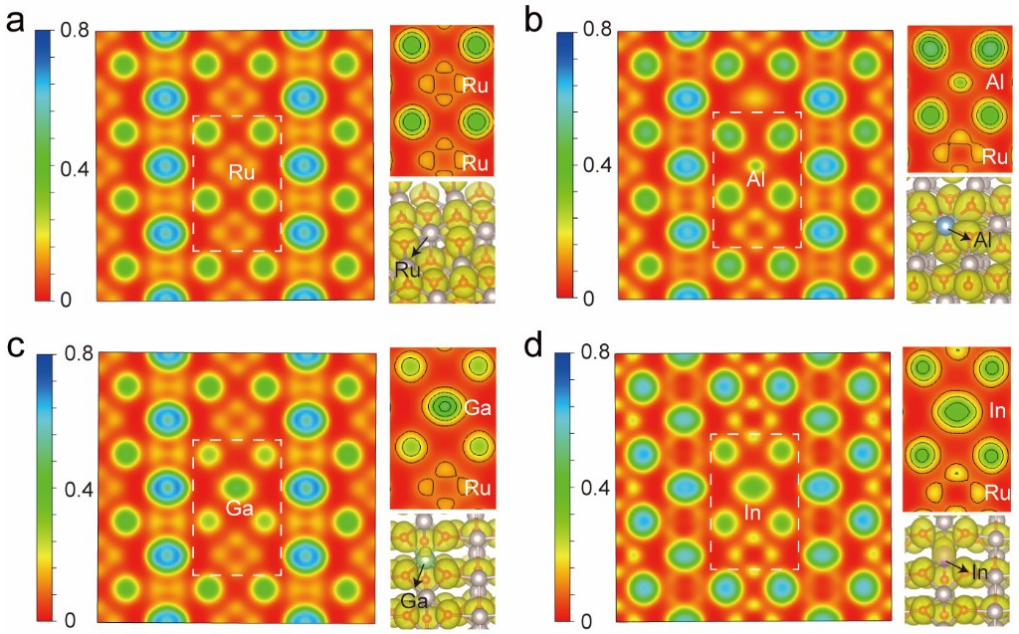


**Fig. S36** The two-dimensional electron localization function (ELF) maps of (a) $RuO_2$, (b) Al-$RuO_2$, (c) Ga-$RuO_2$ and (d) In-$RuO_2$.

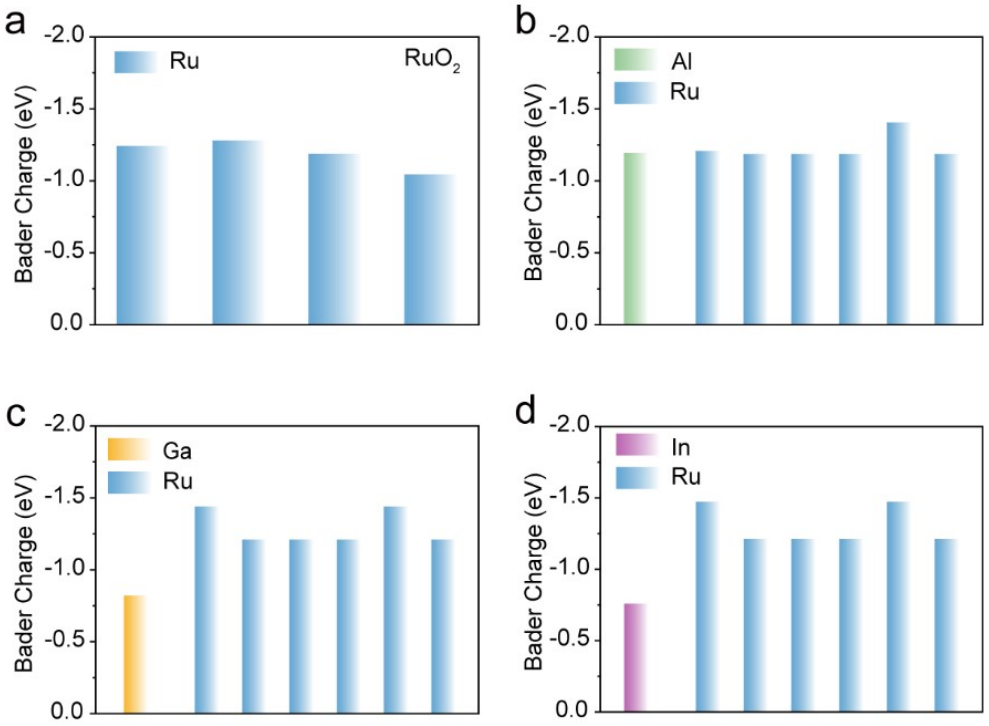


**Fig. S37** The Bader charge of (a) $RuO_2$, (b) Al-$RuO_2$, (c) Ga-$RuO_2$ and (d) In-$RuO_2$.

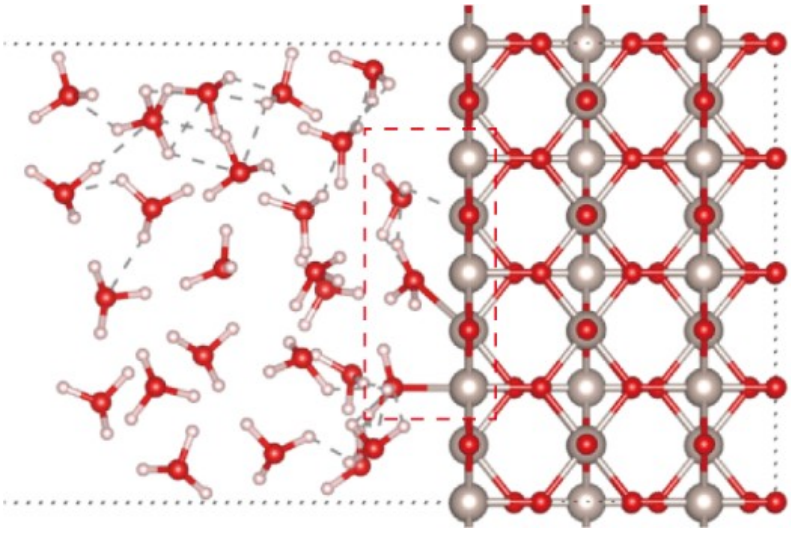

**Fig. S38** The solvation model of $RuO_2$.

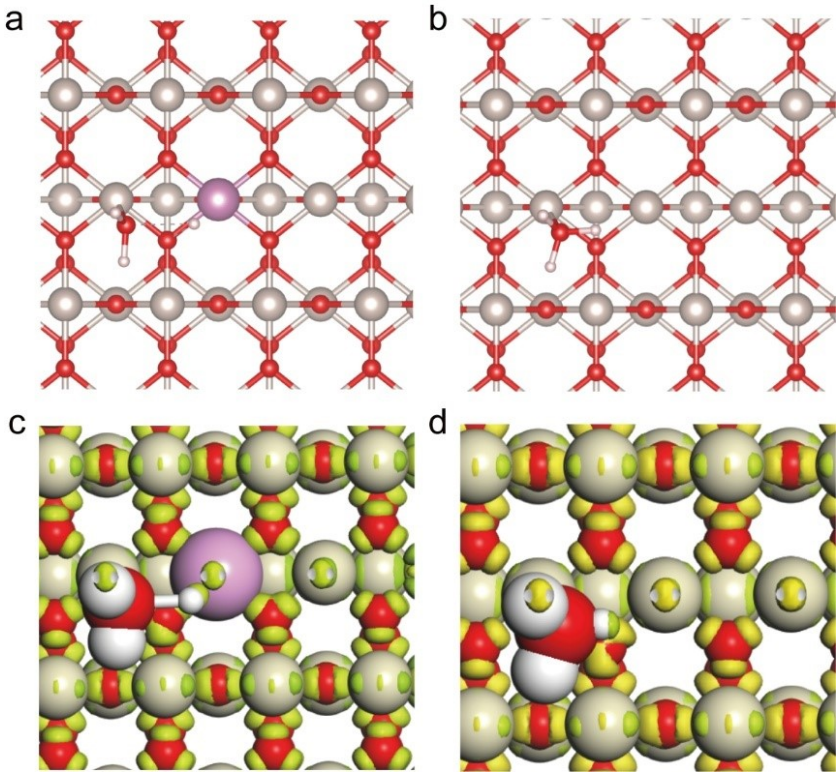


**Fig. S39** The water adsorption model of In-$RuO_2$ and $RuO_2$.

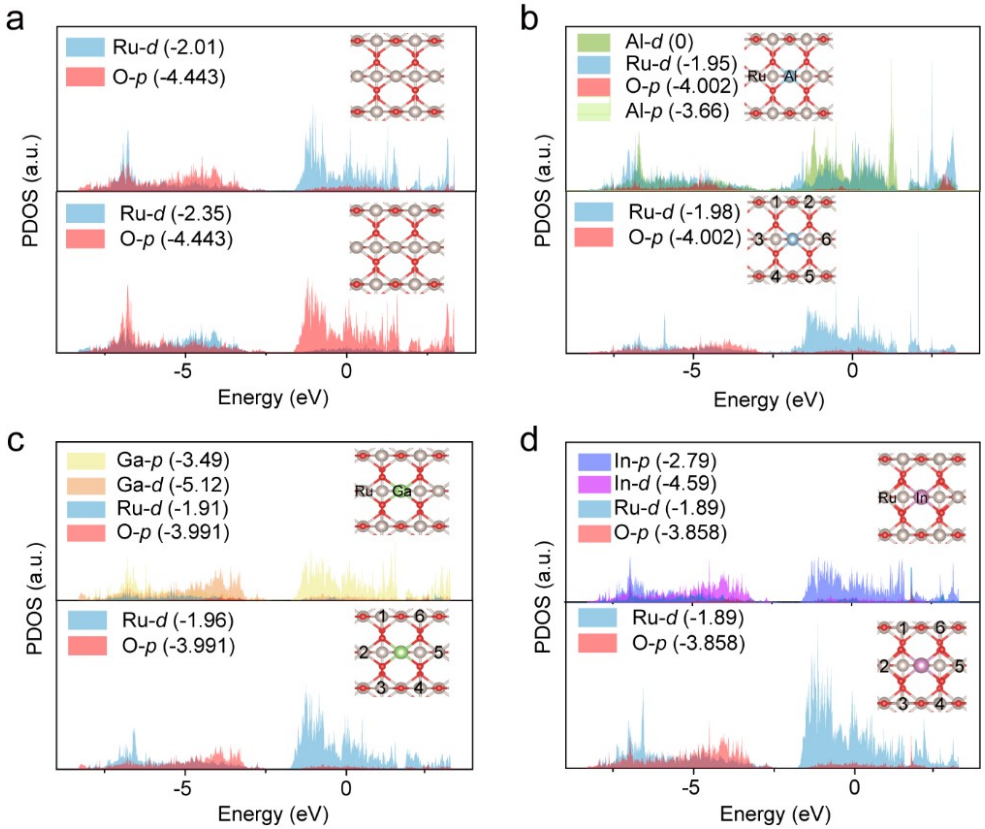


**Fig. S40** The PDOS of (a) $RuO_2$, (b) Al-$RuO_2$, (c) Ga-$RuO_2$ and (d) In-$RuO_2$.

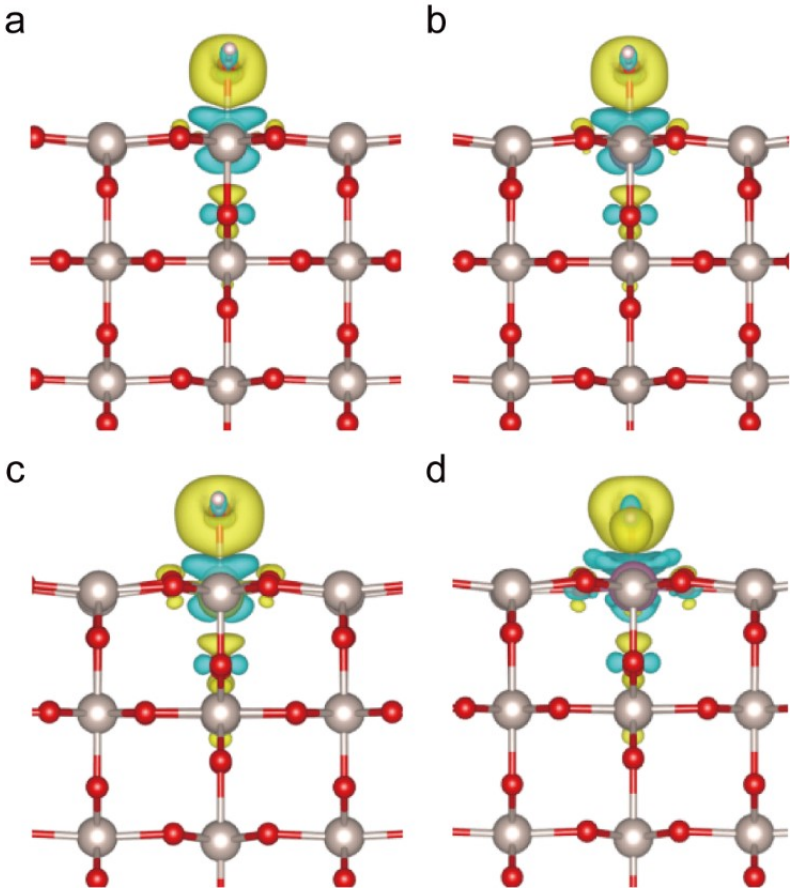


**Fig. S41** Differential charge density of (a) $RuO_2$, (b) Al-$RuO_2$, (c) Ga-$RuO_2$ and (d) In-$RuO_2$.

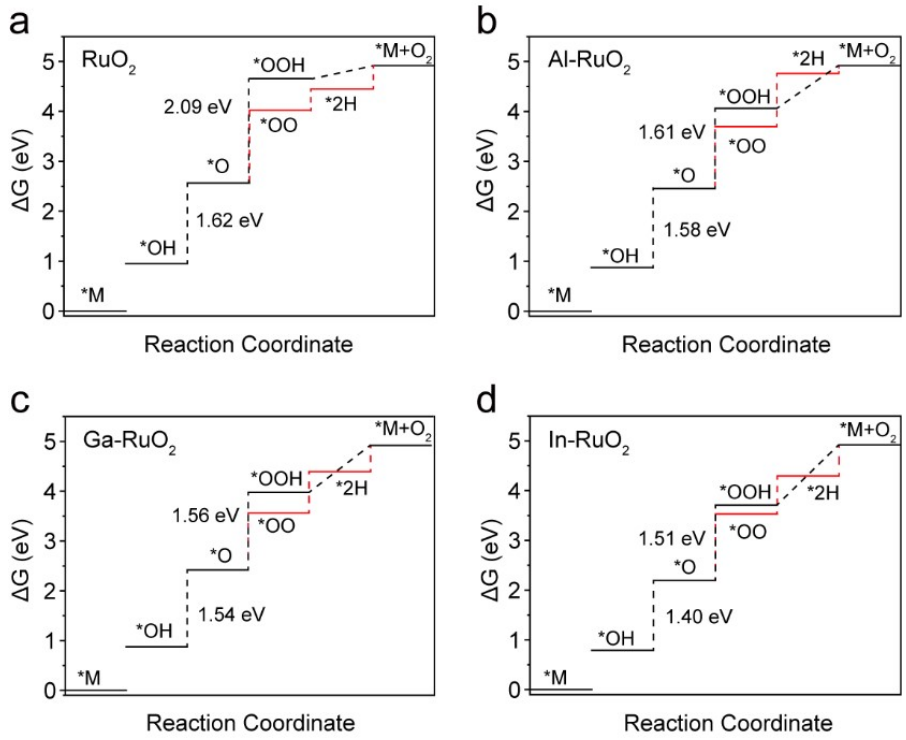


**Fig. S42** The Gibbs free energy diagram of (a) $RuO_2$, (b) Al-$RuO_2$, (c) Ga-$RuO_2$ and (d) In-$RuO_2$.

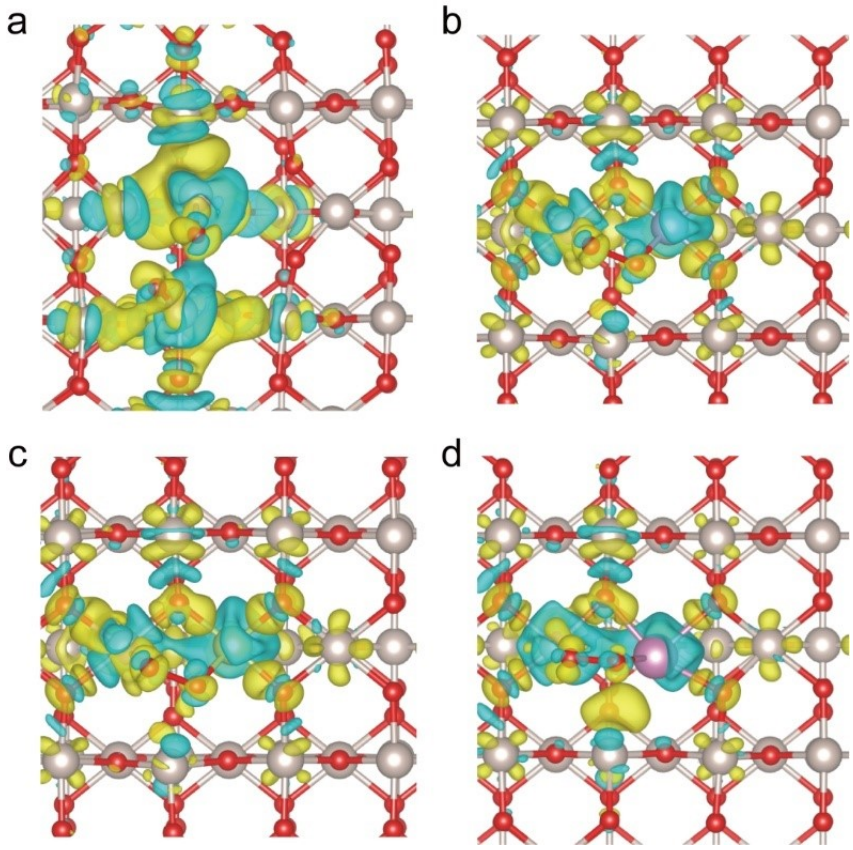


**Fig. S43** Differential charge density of (a) $RuO_2$, (b) Al-$RuO_2$, (c) Ga-$RuO_2$ and (d) In-$RuO_2$ after oxygen vacancies formation.

**Table S1** Structural parameters extracted from the Ru K-edge EXAFS fitting. ($S_0^2$=0.69).

| Catalysts | shell | CN | R(Å) | $\sigma^2$ | $\Delta E_0$ | R factor |
|---|---|---|---|---|---|---|
| Ru foil | Ru-Ru | 12 | 2.667 | 0.00306 | -6.216 | 0.014 |
| $RuO_2$ | Ru-$O_1$ | 6 | 1.958 | 0.00169 | -2.348 | 0.063 |
| | Ru-Ru | 6 | 3.117 | 0.00043 | | |
| | Ru-$Ru_2$ | 2 | 3.544 | 0.00058 | | |
| In-$RuO_2$ | Ru-$O_1$ | 5.83 | 1.967 | 0.00342 | -5.289 | 0.057 |
| | Ru-Ru | 4.22 | 3.132 | 0.00308 | | |
| | Ru-$Ru_2$ | 1.85 | 3.549 | 0.00199 | | |

For the EXAFS fitting, $S_0^2$ is the amplitude reduction factor; R is interatomic distance (the bond length between Ru central atoms and surrounding Ru atoms or coordination oxygen atoms); $\sigma^2$ is Debye-Waller factor (a measure of thermal and static disorder in absorber-scatterer distances); $\Delta E_0$ is edge-energy shift (the difference between the zero kinetic energy value of the sample and that of the theoretical model). R factor is used to value the goodness of the fitting. Data ranges: $3 \leq K \leq 12$ Å$^{-1}$, $1.0 \leq R \leq 4.0$ Å.

**Table S2** Fitting results of the O 1s XPS spectra for the $RuO_2$, Al-$RuO_2$, Ga-$RuO_2$, and In-$RuO_2$ catalysts.

| Sample | Peak | Position(eV) | Area | $OH_{ads}$ content/at% |
|---|---|---|---|---|
| | Lattice O | 529.67 | 4912.54 | |
| **$RuO_2$** | $OH_{ads}$ | 531.70 | 8536.69 | 41.5 |
| | $H_2O_{ads}$ | 533.23 | 7122.61 | |
| | Lattice O | 529.72 | 2605.88 | |
| **Al-$RuO_2$** | $OH_{ads}$ | 531.87 | 9790.73 | 48.1 |
| | $H_2O_{ads}$ | 533.35 | 7956.49 | |
| | Lattice O | 529.74 | 3744.25 | |
| **Ga-$RuO_2$** | $OH_{ads}$ | 532.01 | 13535.64 | 52.7 |
| | $H_2O_{ads}$ | 533.60 | 8411.44 | |
| | Lattice O | 529.30 | 1993.77 | |
| **In-$RuO_2$** | $OH_{ads}$ | 531.80 | 16592.02 | 63.0 |
| | $H_2O_{ads}$ | 533.28 | 7734.55 | |

**Table S3** Comparisons of In-$RuO_2$ with other representative OER catalysts reported under acidic conditions in a three-electrode system.

| Catalysts | *j* (mA $cm^{-2}$) | Electrolyte | η (mV) | Reference |
|---|---|---|---|---|
| In-$RuO_2$ | 10 | 0.5 M $H_2SO_4$ | 194 | This work |
| $Ru_{1-x}O_2$ | 10 | 0.5 M $H_2SO_4$ | 212 | [1] |
| 4*f*-Nd-$RuO_2$ | 10 | 0.1 M $HClO_4$ | 214 | [2] |
| Na/Hf-$RuO_2$ | 10 | 0.5 M $H_2SO_4$ | 238 | [3] |
| Pt-$RuO_2$ | 10 | 0.5 M $H_2SO_4$ | 215 | [4] |
| Ur-Se-$RuO_x$ | 10 | 0.5 M $H_2SO_4$ | 226 | [5] |
| $RuO_2$@COF-O(3) | 10 | 0.5 M $H_2SO_4$ | 218 | [6] |
| a-$TiO_2$/o-$RuO_x$ | 10 | 1.0 M $HClO_4$ | 213 | [7] |
| Mn-$RuO_2$ | 10 | 0.5 M $H_2SO_4$ | 213 | [8] |
| $IrRu_{2.5}/MnTiO_3$ | 10 | 0.5 M $H_2SO_4$ | 165 | [9] |
| $Bi_{0.05}Ru_{0.95}O_2$ | 10 | 0.5 M $H_2SO_4$ | 203 | [10] |
| Sm-$RuO_2$ | 10 | 0.5 M $H_2SO_4$ | 219 | [11] |
| COF-205-Ru | 10 | 0.5 M $H_2SO_4$ | 210 | [12] |
| $Co_3O_4$ / Ni-$RuO_2$ / rGO | 10 | 0.5 M $H_2SO_4$ | 195 | [13] |
| Ru/$RuO_2$ | 10 | 0.5 M $H_2SO_4$ | 183 | [14] |
| $Nb_{0.1}Mn_{0.1}Ru_{0.8}O_2$ | 10 | 0.5 M $H_2SO_4$ | 209 | [4] |

**Table S4.** ICP-MS data for In-$RuO_2$ during 60 h stability testing.

| | Time (h) | The concentration of Ru (ppb) |
|---|---|---|
| **In-$RuO_2$** | 12 | 21.1265 |
| | 24 | 25.5855 |
| | 36 | 29.0145 |
| | 48 | 33.677 |
| | 60 | 37.866 |

**Table S5** Comparison of the performance of In-$RuO_2$ as the anode in PEMWE with the reported Ru/Ir-based catalysts.

| Catalysts | Membrane type | Electrolyte | Cell voltage | Stability | Temperature | Ref |
|---|---|---|---|---|---|---|
| In-$RuO_2$ | Nafion®117 | 0.5 M $H_2SO_4$ | 1.67 V @ 1 A $cm^{-2}$ | 1000 h @ 1 A $cm^{-2}$ | 80 °C | This work |
| Er-$RuO_x$ | Nafion®117 | 0.5 M $H_2SO_4$ | 1.84 V @ 3 A $cm^{-2}$ | 100 h @ 500 mA $cm^{-2}$ | 80 °C | [15] |
| $Ru_{0.8}Sb_{0.2}O_2$ | Nafion®117 | 0.5 M $H_2SO_4$ | 1.64 V @ 1 A $cm^{-2}$ | 1160 h @ 1 A $cm^{-2}$ | 80 °C | [16] |
| $H_{3.8}Ir_{1-x}Ru_xO_4$ | Nafion®117 | 0.5 M $H_2SO_4$ | 1.78 V @ 1 A $cm^{-2}$ | 80 h @ 100 mA $cm^{-2}$ | 80 °C | [17] |
| m-$RuO_2$ | Nafion®115 | 0.5 M $H_2SO_4$ | 1.72 V @ 1 A $cm^{-2}$ | 100 h @ 1 A $cm^{-2}$ | 80 °C | [18] |
| $ZnRuO_x$ | Nafion®211 | 0.5 M $H_2SO_4$ | 1.68 V @ 1 A $cm^{-2}$ | 120 h @ 200 mA $cm^{-2}$ | 80 °C | [19] |
| IrRu NWs | Nafion®117 | 0.5 M $H_2SO_4$ | 2.0 V @ 2.6 A $cm^{-2}$ | 500 h @ 1 A $cm^{-2}$ | 80 °C | [20] |
| Mn-$RuO_2$ | Nafion®115 | 0.5 M $H_2SO_4$ | 1.72 V @ 1 A $cm^{-2}$ | 200 h @ 100 mA $cm^{-2}$ | 80 °C | [21] |

| | | | | | | |
|---|---|---|---|---|---|---|
| $RuO_2$/LiCoO$_2$ | Nafion®115 | 0.5 M $H_2SO_4$ | 1.68V @ 1 A $cm^{-2}$ | 2000 h @ 1 A $cm^{-2}$ | 80 °C | [22] |
| Mn-$RuO_2$ | Nafion®115 | 0.5 M $H_2SO_4$ | 1.78 V @ 1 A $cm^{-2}$ | 180 h @ 1 A $cm^{-2}$ | 80 °C | [8] |
| a-Ge-$RuO_2$ | Nafion®115 | 0.5 M $H_2SO_4$ | 1.62 V @ 1 A $cm^{-2}$ | 400 h @ 200 mA $cm^{-2}$ | 60 °C | [23] |
| RuFe@CF | Nafion®115 | 0.5 M $H_2SO_4$ | 1.898 V @ 1 A $cm^{-2}$ | 250 h @ 200 mA $cm^{-2}$ | 60 °C | [24] |

**Table S6** The infrared peak positions and proportions of different types of interfacial water on $RuO_2$ catalysts.

| **Potential (V)** | **4-HB·$H_2O$ proportion (%)** | **2-HB·$H_2O$ Proportion (%)** | **Free $H_2O$ Proportion (%)** |
|---|---|---|---|
| **1.3** | 45.2 | 45.1 | 9.6 |
| **1.4** | 45.7 | 44.3 | 10.0 |
| **1.5** | 45.6 | 45.0 | 9.4 |
| **1.6** | 45.3 | 45.6 | 9.1 |
| **1.7** | 45.3 | 46.0 | 8.7 |
| **1.8** | 44.8 | 47.0 | 8.2 |

**Table S7** The infrared peak positions and proportions of different types of interfacial water on Al-$RuO_2$ catalysts.

| **Potential (V)** | **4-HB·$H_2O$ proportion (%)** | **2-HB·$H_2O$ proportion (%)** | **Free $H_2O$ proportion (%)** |
|---|---|---|---|
| **1.3** | 47.4 | 44.8 | 7.8 |
| **1.4** | 48.2 | 43.5 | 8.3 |
| **1.5** | 48.6 | 42.6 | 8.8 |
| **1.6** | 49.1 | 41.7 | 9.2 |
| **1.7** | 49.9 | 40.1 | 10 |
| **1.8** | 49.0 | 40.5 | 10.5 |

**Table S8** The infrared peak positions and proportions of different types of interfacial water on Ga-$RuO_2$ catalysts.

| **Potential (V)** | **4-HB·$H_2O$ Proportion (%)** | **2-HB·$H_2O$ Proportion (%)** | **Free $H_2O$ Proportion (%)** |
|---|---|---|---|
| **1.3** | 48.1 | 43.5 | 8.4 |
| **1.4** | 48.5 | 42.1 | 9.4 |
| **1.5** | 48.9 | 40.1 | 11.0 |
| **1.6** | 49.3 | 39.6 | 11.1 |
| **1.7** | 50.1 | 38.3 | 11.6 |
| **1.8** | 50.4 | 38.5 | 11.1 |

**Table S9** The infrared peak positions and proportions of different types of interfacial water on In-$RuO_2$ catalysts.

| **Potential (V)** | **4-HB·$H_2O$ Proportion (%)** | **2-HB·$H_2O$ Proportion (%)** | **Free $H_2O$ Proportion (%)** |
|---|---|---|---|
| **1.3** | 53.4 | 37.4 | 8.7 |
| **1.4** | 55.4 | 34.8 | 9.8 |
| **1.5** | 56.5 | 32.6 | 10.9 |
| **1.6** | 58.0 | 30.6 | 11.4 |
| **1.7** | 59.0 | 28.7 | 12.3 |
| **1.8** | 60.2 | 27.3 | 12.5 |

## References


1 J. Yang, K. An, Z. Yu, L. Qiao, Y. Cao, Y. Zhuang, C. Liu, L. Li, L. Peng and H. Pan, *ACS Catal.*, 2024, **14**, 17739–17747.

2 X. Zhang, Y. Zhang, B. O. Protsenko, M. A. Soldatov, J. Zhang, C. Yang, S. Bo, H. Wang, X. Chen, C. Wang, W. Cheng and Q. Liu, *Nat. Commun.*, 2025, **16**, 16:6921.

3 Y. a. Zhu, F. Wu, X. Zhang, Y. Lin, L. Zhang, T. S. Chan, Q. Zhang and L. Chen, *Adv. Mater.*, 2025, **37**, 2500449.

4 X. Cao, L. Miao, W. Jia, H. Qin, G. Lin, R. Ma, T. Jin and L. Jiao, *Nat. Commun.*, 2025, **16**, 16:6217.

5 Y. Yang, S. Wang, G. Zhang, X. Li, Q. Wu, H. Liu, Z. Deng, X. Han, S. Zhang, W. Dong, J. Song, Y. Chen, X. Gao, Y. Yang, J. Dong, L. Cao and Z. Zhao, *Angew. Chem. Int. Ed.*, 2025, **64**, e202512848.

6 K. Wang, S. Xu, D. Wang, Z. Kou, Y. Fu, M. Bielejewski, V. Montes-García, B. Han, A. Ciesielski, Y. Hou and P. Samorì, *Adv. Mater.*, 2025, **37**, 2417374.

7 C. J. Soderstedt, Y. Yuan, S. A. Vigil, H. H. Ford, M. Fratarcangeli, Z. Lin, J. G. Chen and I. A. Moreno-Hernandez, *J. Am. Chem. Soc.*, 2025, **147**, 24502–24509.

8 Z.-H. Xue, J. Mahmood, Y. Shang, G. Li, S.-J. Kim, Y. Han and C. T. Yavuz, *J. Am. Chem. Soc.*, 2025, **147**, 17839–17848.

9 J. Chen, J. Yang, Y. Han, Y. Huang, N. Tian, J. Li and Z. Wang, *ACS Catal.*, 2025, **15**, 14882–14894.

10 S. Chen, H. Liu, B. Yuan, W. Xu, A. Cao, M. G. Sendeku, Y. Li, X. Sun and F. Wang, *Nanoscale*, 2024, **16**, 20940–20947.

11 B. Du, W. Li, Z. Yan, S. Shu, G. Ma, B. Guo and S. Li, *Dalton Transactions*, 2025, **54**, 15833–15841.

12 H. Jia, N. Yao, Y. Jin, L. Wu, J. Zhu and W. Luo, *Nat. Commun.*, 2024, **15**, 15:5419.

13 W. Yang, Z. Wang, J. Zhang, L. Jia, J. Li, X. Chen, X. Liu, H. Zhang, J. Lin, M. Zhao and Q. Chen, *Angew. Chem. Int. Ed.*, 2025, **64**, e202509768.

14 Q. Lu, J. Liu, X. Zou, B. Huang, W. Wu, J. Yin, Z. Q. Liu and Y. Wang, *Angew. Chem. Int. Ed.*, 2025, **64**, e202503733.

15 L. Li, G. Zhang, C. Zhou, F. Lv, Y. Tan, Y. Han, H. Luo, D. Wang, Y. Liu, C. Shang, L. Zeng, Q. Huang, R. Zeng, N. Ye, M. Luo and S. Guo, *Nat. Commun.*, 2024, **15**, 15:4974.

16 L. Deng, S.-F. Hung, S. Liu, S. Zhao, Z.-Y. Lin, C. Zhang, Y. Zhang, A.-Y. Wang, H.-Y. Chen, J. Peng, R. Ma, L. Jiao, F. Hu, L. Li and S. Peng, *J. Am. Chem. Soc.*, 2024, **146**, 23146–23157.

17 J. Tang, X. Liu, X. Xiong, Q. Zeng, Y. Ji, C. Liu, J. Li, H. Zeng, Y. Dai, X. Zhang, C. Li, H. Peng, Q. Jiang, T. Zheng, C. W. Pao and C. Xia, *Adv. Mater.*, 2024, **36**, 2407394.

18 G. Zhao, W. Guo, M. Shan, Y. Fang, G. Wang, M. Gao, Y. Liu, H. Pan and W. Sun, *Adv. Mater.*, 2024, **36**, 2404213.

19 P. Sun, Z. Qiao, X. Dong, R. Jiang, Z.-T. Hu, J. Yun and D. Cao, *J. Am. Chem. Soc.*, 2024, **146**, 15515–15524.
20 B. Pang, S. Feng, Y. Xu, H. Chen, J. Li, Y. Yuan, X. Zou, X. Tian and Z. Kang, *Adv. Funct. Mater.*, 2024, **34**, 2411062.
21 X. Zhou, Z. Yang, Y. Qian, Z. Luo, L. Zhang, Q. Zhang, C. He, Z. Luo and X. Ren, *Journal of Energy Chemistry*, 2026, **112**, 967–976.
22 L. Wang, S.-F. Hung, S. Zhao, Y. Wang, S. Bi, S. Li, J.-J. Ma, C. Zhang, Y. Zhang, L. Li, T.-Y. Chen, H.-Y. Chen, F. Hu, Y. Wu and S. Peng, *Nat. Commun.*, 2025, **16**, 16:3502.
23 T. Xu, Q. Liang, F. Liu, Z. Zhao, W. Li, A. Wei, M. Liu, K. Song, B. Yang, T. Dong, X. Zou, W. Zhang and W. Zheng, *Adv. Funct. Mater.*, 2025, https://doi.org/10.1002/adfm.202522894e22894.
24 J. Chen, Y. Ma, T. Huang, T. Jiang, S. Park, J. Xu, X. Wang, Q. Peng, S. Liu, G. Wang and W. Chen, *Adv. Mater.*, 2024, **36**, 2312369.